POLITECNICO DI TORINO

Department of Mechanical and Aerospace Engineering

Masters of Science Degree in Mechanical Engineering

NUMERICAL SIMULATION of DEFORMABLE RADIAL JOURNAL BEARINGS

Supervisors

Prof. Cristiana DELPRETE

Prof. Chiara GASTALDI

Candidate

AHMAD MOHAMAD

March 2021

Abstract

Hydrodynamic journal bearings are used as load carrying capacitors where fluid is used as a lubricant between the rotating shaft and the bearing. This causes pressure to increase in the lubricant gap, and thus plays an important role in supporting the loads. In this work, we use a three-dimensional model to numerically compute the pressure distribution inside the lubricant gap in order to estimate the load carrying capacity of the journal bearing. The analytical solutions were based on Reynolds equation, but limited to infinitely long/short bearings in order to find accurate results. The numerical simulation is carried out using ANSYS software to examine two main cases; In the first case, both the shaft and the bearing are treated as rigid bodies while the second case highlights the effect of the shaft and the bearings' deformations on the pressure distribution. When comparing both cases, we noticed that the latter generated more accurate results for the pressure distribution and a better estimate of the maximum pressure (lower values) inside the lubricant gap. Moreover, we analyzed the effect of increasing the shaft rotational speed and the eccentricity ratio on the pressure values. The final results show an increase in the maximum pressure with the increase of rotational speed and eccentricity ratio.

Acknowledgements

I would like to send my gratitude to my supervisors Prof Cristiana Delprete and Prof. Chiara Gastaldi for their guidance and support throughout the whole thesis. Their assistance helped me to understand and present the theory part of the thesis in the best way. Moreover, their help in the numerical part was very important for me to understand and complete the simulations presented in the work.

In addition I thank my family and my parents for giving me the support and love. Without them I would never be able to complete my work and reach this level of success.

Table of Contents

List of Tables

List of Figures

Chapter 1

Introduction

1.1 Background

The bearing is a machine element used to constraint motion and reduces the friction between moving parts. Bearings are classified into several types according to their shapes. There are contact bearings, such as ball and roller bearings, in which rolling elements (balls and rollers) are used for reducing friction and holding the rotating components [1] . Other type of bearings is the hydrodynamic journal bearings. They are widely used and have an advantage over other types of bearings because of their higher load carrying capacity and higher operating angular speeds. Also they have lower cost, higher durability, better damping characteristics and easier manufacturing [2].The working principle of these bearings is governed by the lubricating oil fed to the bearing. The lubricant plays the role of separating the moving shaft and the bearing itself. When the oil is supplied into the lubricant gap, the rotation of the shaft continuously provides energy to the oil. As a result, pressure is created inside the lubricant (oil), which allows the load support. The word “bearing” mean to bear or to support. It bears the forces, mainly axial forces, to maintain the shaft in its position and decrease friction between parts as well as noise. Although heat dissipation created by the journal bearing work decreases the efficiency the system, but it increases the overall performance. The lubricant is supplied and a thin film between the journal (shaft) and the bearing is created. The load carrying capacity of the thin film is represented by the pressure distribution inside the film. The pressure created inside the lubricant gap has the role of supporting loads and decreasing friction [3]. In order to find the pressure distribution inside the oil lubricant, scientists used Reynolds equation. The equation is derived from Navier-Stokes and continuity equations. The analytical solution of Reynolds equation is oversimplified, and it is obtained only for long/short length of the bearing [4]. In order to have a reasonable results, Reynolds equation should be solved numerically. One the most used numerical software for solving fluid mechanics problems is Fluent.

1.2 Numerical Method

Fluent is a Computational Fluid Dynamics (CFD) code used for modeling fluid flow, chemical reactions, heat and mass transfers. It is part of the commercial software ANSYS. It solves the Navier-Stokes and continuity equation to find the pressure distribution along the oil film. First it divides the model into cells called "control volumes", and then it solves the partial differential equations (PED) at each moment for every cell. It works by linearizing these PDE to form a system of linear equations. It is necessary to set suitable boundary conditions and define the properties of the oil and other materials used [5]. Solving the hydrodynamic problem using Fluent gives a results considering the fluid part of the system without including any effect of the mechanical deformations of the solid parts. This could give results with lower accuracy and overestimate the maximum pressure, thus overestimate the load carrying capacity of the journal bearing [6]. To include the effect of deformation of the bearing and/or the journal, a finite structural interaction (FSI) method should be used. The solution can be obtained by coupling the Fluent system with a finite element method (FEM) to account for the effect of deformations on the pressure profile and visa versa.

1.3 Objectives

The objective of the thesis is to investigate the capability of Fluent ANSYS in solving Reynolds equation and finding the pressure distribution along the lubricating oil film. The model is solved in Fluent, without considering the effect of deformations. Then, the model is solved by modeling the elastic deformations of the shaft and the bearing. The results are then compared in terms of accuracy and computational time. In addition, we examine the effect of shaft rotational speed and the eccentricity ratio on the final results.

Chapter 2

Literature Review

2.1 Journal Bearing Modeling

The geometry of the journal bearing system used in this study is shown in the Fig. 2.1. The circular shaft rotates with an angular velocity ω. The shaft has a diameter D which is smaller than the diameter of the bearing surrounding it. The bearing has diameter D' and center C'. In this model, the two circles are not concentric, and the distance between the center of the shaft C and the bearing's center C' is referred as eccentricity e. Also, the radial distance between the shaft and the bearing is called the radial clearance c. In this region, the radial clearance, the lubricant is supplied. The axial length (not shown in the figure) of the bearing is L, and ψ is the attitude angle.

By looking at the same figure, we see that W is the external force acting on the shaft center in the y-direction. Due to this force, the shaft remains in equilibrium position with respect to the eccentricity value. In addition, the region between the shaft and the bearing forms converging and diverging zones. Therefore, Hydrodynamic pressure is created in the convergent zone. The generation of pressure depends on the value of eccentricity, clearance, viscosity and internal surface geometry. The oil film thickness is a function of clearance, eccentricity and the angle θ.

$$h(\theta) = c + e\cos(\theta) \tag{2.1}$$

θ is measured from the line of centers joining the two centers O and O'. The maximum value of h is related to null θ. For $\theta = \pi$, the thickness h is minimum. The equation of thickness can be written as:

$$h(\theta) = c(1 + \epsilon\cos(\theta)) \tag{2.2}$$

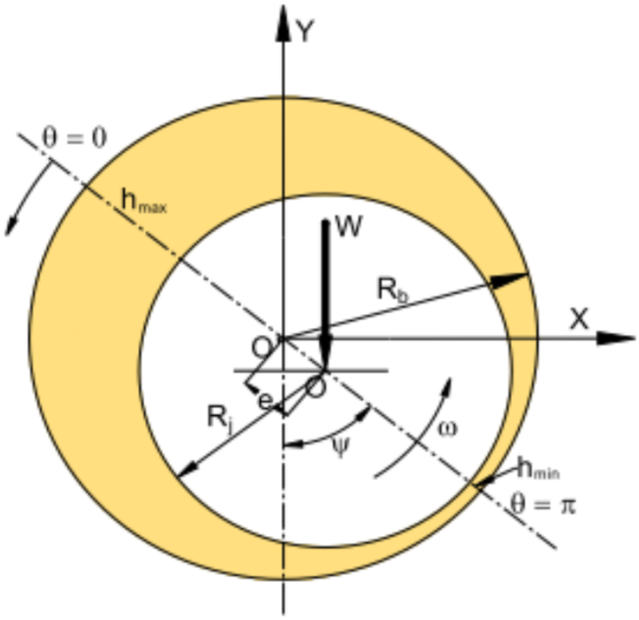

Figure 2.1: Schematic diagram of a journal bearing

where $\epsilon = e/c$ is the eccentricity ratio.

The steady state response of the system can be studied using the Reynolds equation [**8** , 7, 9]. The equation derived from Navier-Stokes equations and the continuity equation.

$$\frac{1}{r^2}\frac{\partial}{\partial s}(\frac{h^3}{\mu}\frac{\partial P}{\partial \theta}) + \frac{\partial}{\partial z}(\frac{h^3}{\mu}\frac{\partial P}{\partial z}) = 6\frac{U}{r}\frac{\mathrm{d}h}{\mathrm{d}\theta} \tag{2.3}$$

where $U = \omega r$ is the tangential velocity of shaft and μ is the fluid dynamic viscosity

The assumptions we consider when we apply this equation are:

- The equation is used for both compressible and incompressible fluids.
- Negligible inertia and body forces compared to pressure and viscos forces.
- No slip at the solid boundaries of the fluid.
- Pressure is constant across the oil film.
- No external forces act on the fluid.

- Laminar flow.
- Only derivatives in the y direction of u and w are considered, others are negligible.

In this work, the solution is based on full Navier-Stokes equations:

$$\rho\frac{\partial u}{\partial t} = -\frac{\partial P}{\partial x} + \nabla(\mu\triangle u) + S_{Mx} \tag{2.4}$$

$$\rho\frac{\partial v}{\partial t} = -\frac{\partial P}{\partial y} + \nabla(\mu\triangle v) + S_{My} \tag{2.5}$$

$$\rho\frac{\partial w}{\partial t} = -\frac{\partial P}{\partial z} + \nabla(\mu\triangle w) + S_{Mz} \tag{2.6}$$

Along with the continuity equation:

$$\frac{\partial \rho}{\partial t} + \triangle(\rho\vec{v}) = 0 \tag{2.7}$$

ρ is the fluid density and $\vec{v}$ is the fluid velocity vector.

As well as the Momentum equation:

$$\frac{\partial}{\partial t}(\rho\vec{v}) + \nabla(\rho\vec{v}\vec{v}) = -\nabla P + \nabla(\overline{\overline{z}}) + \rho\vec{g} + \vec{F} \tag{2.8}$$

z is the static tensor, $\rho\vec{v}$ is the gravitational force and $\vec{F}$ is the external force. Also, the 3D energy equation is written as:

$$\frac{\partial}{\partial t}(\rho C_p T) + \nabla(\rho\vec{v}C_p T) = \nabla(KVT) + Q_v \tag{2.9}$$

These equations are solved using Fluent depending on the geometry, materials properties and boundary conditions.

2.2 Two Dimensional (2D) and three Dimensional Models (3D)

In order to solve the Navier-Stokes and Reynolds equation related to the journal bearing being under study, different commercial codes could be used based on considering 2D or 3D models. The main reason behind using 2D model is the lower computation cost in terms of time [7]. The flow in 2D model is also 2D, so it neglects the change in the third direction of the fluid flow. This may give reasonable results if the actual flow of the fluid in the model is almost 2D, otherwise 3D simulation should be used [10]. Even if the 2D model gives accurate results in the cases that we can use 2D simulation, the results given by 3D model are more realistic, because they consider the actual geometry and the actual flow of the fluid along with the variation of the flow in the three directions, not only two directions [11]. We can expect the middle layer of the 3D model to be quite similar to the results obtained in 2D model, but the outer layers are different. The reason behind this difference, other than considering only 2D flow, is not considering the actual boundary conditions in 2D model, because they depend on the type of geometry, and 3D boundary conditions are more realistic [12]. Considering the effect of deformation on the pressure and temperature distribution, the use of 2D model is not accurate; as a result, we have to use 3D model to represent the effects of elastic deformations as well as pressure and temperature variations. The deformation of the shaft and the journal should be considered using 3D geometry. These deformations as well as their effect on the fluid flow cannot be represented by 2D model.

The necessity for using 3D simulation for journal bearings is justified when considering the effect of cavitation. Cavitation occurs at very high loads, by which a phase change happens by shifting from liquid to vapour when the pressure goes down below the fluid's vapour pressure [13]. In this case, two phase of the liquid is created in the area of the cavitation. The vapor forms a three dimensional layer across the film. 2D methods cannot represent these areas and the simulation of the journal bearings considering the effect of cavitation should be done using 3D models. In [12], a comparison between 2D and 3D simulation of journal bearing is done in order to show the difference between the results of the 2 types of simulation in terms of surface temperature profile and the oil film thickness distribution for each case. The characteristics of the lubricant performance are different depending on each model. 2D model neglects the heat conduction in axial direction, as well as the viscosity variation in that direction. For the temperature variation, the maximum spot temperature for 3D model appears at the inner outlet, while for 2D model, there is no max spot temperature as seen in Figs.2.2 and 2.3. The 3D model shows a closed temperature field, while the maximum temperature is close to the oil outlet side for 2D model. The presence of closed temperature field is more realistic because it models the heat conduction across the oil film in all directions.

By considering the oil film thickness distribution, for 3D model, we see that a closed film thickness exists; whereas a half closed film thickness appears for 2D model (see Figs.2.4 and 2.5. Also the minimum film thickness is about 14% higher for 2D model compared to 3D model minimum film thickness. The minimum film thickness should not be overestimated because it would be not safe for the journal bearing.

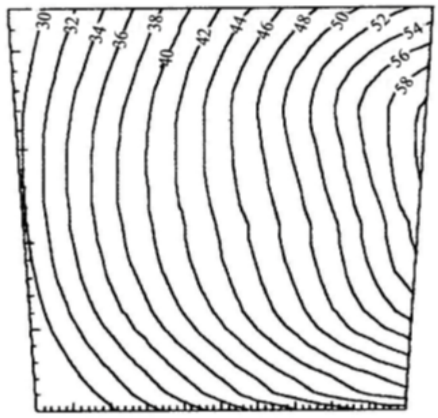

Figure 2.2: 2D temperature field

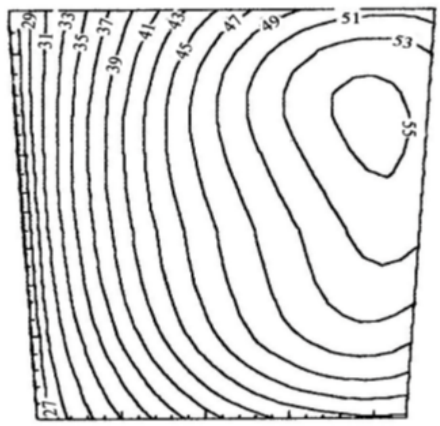

Figure 2.3: 3D temperature field

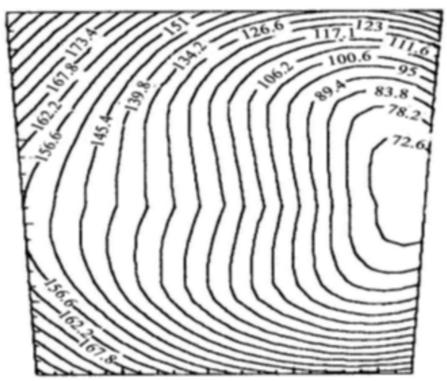

Figure 2.4: 2D film thickness field

Figure 2.5: 3D film thickness field

2.3 Temperature and Pressure effect on Viscosity

By solving the Navier-Stokes equations, pressure distribution is found across the oil film. Many researchers considered constant oil viscosity when solving these equations. [13, 14, 15]. In reality, the viscosity is not constant, and it is affected mainly by the change in temperature and pressure. The temperature and pressure are not constant and they change across the lubricating film and they affect the value of viscosity which will affect the pressure distribution obtained [16]. Due to high load and high speeds, the heat is generated, and as a result, the temperature will increase [16], thus the viscosity of the oil would decrease as a result. For some cases, an increase of $25°C$ can cause an 80% decrease in viscosity [17]. So the viscosity dependence on temperature should be considered to better estimate the pressure and temperature distribution across the oil film, especially for high temperature values. There are several equations describing the viscosity-temperature and viscosity-pressure relationships. Some were purely empirical, while others were derived from theoretical models. One of these equations, which is used in ANSYS Fluent is:

$$\mu = \mu_0 e^{\alpha(p-p_0)} \exp^{\beta(t-t_0)} \tag{2.10}$$

This equation has been appended to ANSYS Fluent using C-Program.

To emphasis the effect of considering this relationship, simulation of journal bearing is done to find the pressure distribution across the oil film [18]. First, two cases were considered, one with constant viscosity and the other with pressure-dependent viscosity.

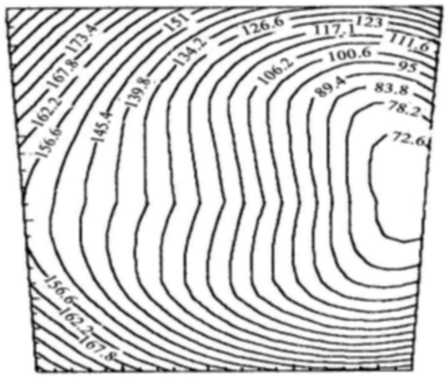

Figure 2.6: Iso-Thermal Pressure

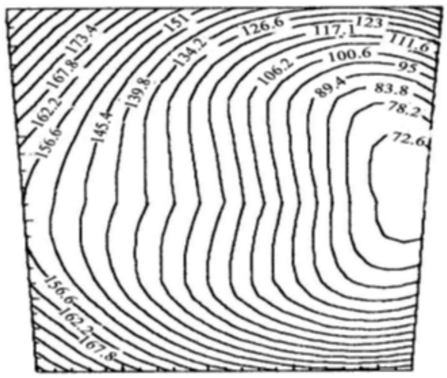

Figure 2.7: Thermal Pressure

The maximum pressure is higher in case of constant viscosity as shown in Fig 2.6 and 2.7. Then, two other cases were considered, with constant and temperature-dependent viscosity.

In these cases, shown in Fig. 2.8 and 2.9, the maximum pressure is also higher for the case of constant viscosity.
In other cases, Vogel and Barus equations are used, which relate viscosity to temperature and pressure respectively [2].

Vogel is written as:

$$\mu = a.\exp^{(b/(T-c))} \tag{2.11}$$

where a, b, c are oil characteristic parameters.

Barus is written as:

$$\mu = \mu_0.\exp^{\alpha p} \tag{2.12}$$

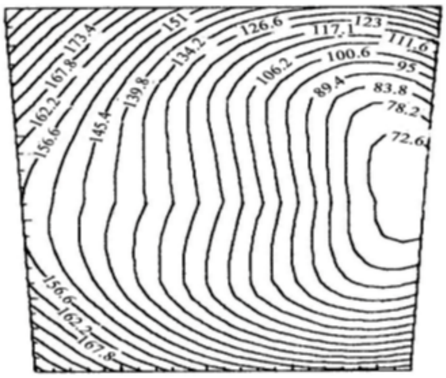

Figure 2.8: Iso-Thermal Temperature

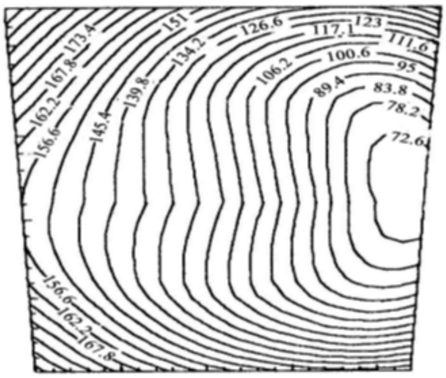

Figure 2.9: Thermal Temperature

Where μ_0 is the viscosity at ambient atmospheric pressure, and α is the pressure viscosity coefficient with typical values 0.01 to 0.02. The temperature of the system could be considered constant, by taking the mean value between the inlet and outlet temperatures, or by considering a linear relation between the two temperature values. For a 3D Model, four cases where considered: constant mean temperature and $\alpha = 0$, constant mean temperature and $\alpha = 0.01$, linear temperature and $\alpha = 0$, and linear temperature and $\alpha = 0.01$ [2] The maximum pressure for each case is different with a highest value for the last case.

The effect of the inlet and outlet temperature is of create importance as shown in Figs.2.10, 2.11, 2.12 and 2.13.

In the first two cases, $T_{in} = 40°C$and T$_{out}$ $= 80°C$. While in the other two cases, $T_{in} = 70°C$and $T_{out} = 90°C$. Linear relationship between inlet and outlet temperature is considered for all cases. The maximum pressure is higher in case of viscosity dependence of pressure ($\alpha = 0.01$), but the difference is much higher when

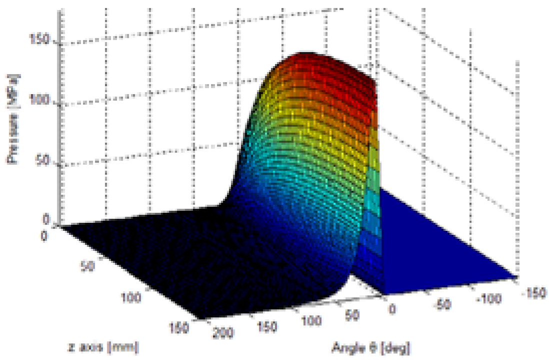

Figure 2.10: Pressure Distribution α =0, P_{max}=179.06 MPa

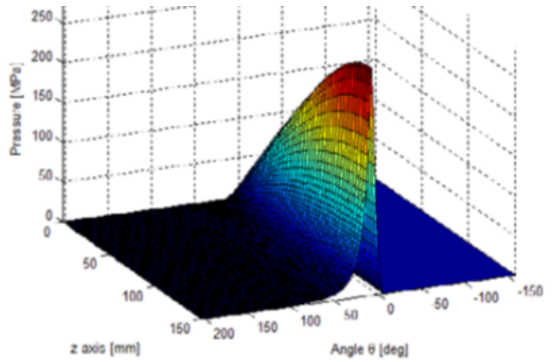

Figure 2.11: Pressure Distribution α=0.01, P_{max}=285.85 MPa

the inlet temperature increases from $40°C$ to $70°C$. Also the shape of pressure distribution profile is different due the effect of viscosity pressure dependence. The effect of temperature and pressure on the viscosity of the lubricating oil is high and depends on the cases of study. To get realistic results, these effects should not be neglected at high pressure and temperature levels.

2.4 Laminar and Turbulent Flow

Many researchers assumed laminar flow in their simulation of hydrodynamic journal bearings [3, 6, 12]. This assumption makes the problem simpler and leads to reasonable results in many cases. Laminar flows are considered for Reynolds number less or near 2300, whereas turbulent flows are related to higher Reynolds number (Re >3000). In numerical simulations, the assumption of laminar flow saves time by decreasing the number of computations for each element. For many cases, especially for journal bearings, this assumption is good choice in terms of time as well as the accuracy of the obtained results. Whereas, on the other side, many other

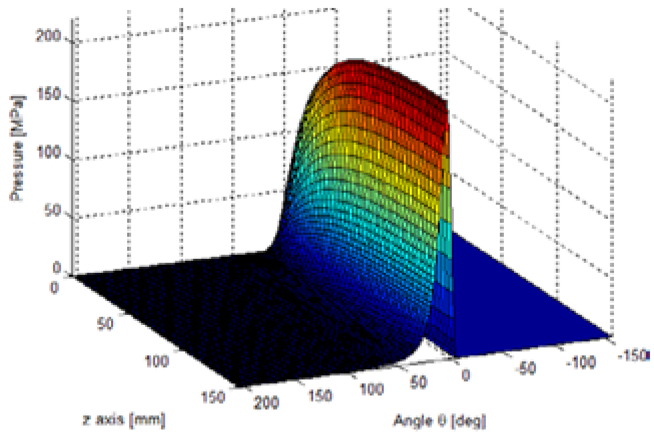

Figure 2.12: Pressure Distribution α=0,P_{max}=221.00 MPa

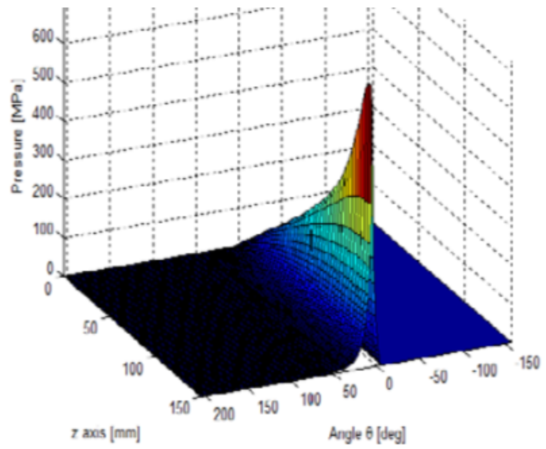

Figure 2.13: Pressure Distribution α=0.01, P_{max}=674.38 MPa

researchers used turbulent flows assumptions to describe their models [19, 20, 21, 22].

To study the effect of laminar/turbulent flow on the numerical simulations of journal bearings, [23] solves the numerical model of journal bearing for three different rotational speeds, under the assumptions of laminar and turbulent flows . The results for each case are obtained in terms of static pressure distribution. For each flow model, the maximum pressure increases by increasing the rotational speed from 3000 to 5000 to 10000 rpm. We can see that the values of the maximum pressure for each rpm are higher in case of turbulent flows. The difference is not high and the results are acceptable. The static pressure is more distributed in case of turbulent flow, but the distribution of pressure shows a similar trend in both cases (as shown in the Fig. 2.14 and 2.15 for the case of 5000 rpm). The static pressure is very low at the beginning, increases gradually to the highest point, and then drops significantly.

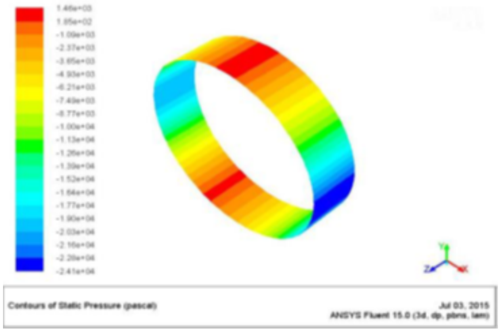

Figure 2.14: Static pressure contour of lubricant for 5000 rpm at turbulent regime

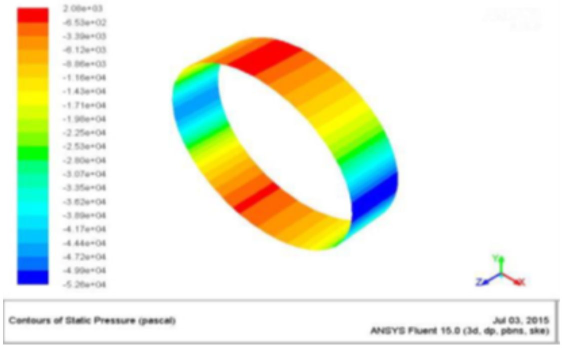

Figure 2.15: Static pressure contour of lubricant for 5000 rpm at laminar regime

It is difficult to determine the best model, laminar or turbulent, and it depends on the case itself. Whereas, in general, the turbulent effect in hydrodynamic journal bearings can be neglected. In some cases, depending on the degree of turbulence, the flow should be modeled as turbulent. For this purpose, different turbulent models are used. Standard k-ϵ model, Realizable k-ϵ model and Reynolds Stress Model (RSM) are three different models used to simulate mean characteristics for turbulent flow conditions.

The standard k-ϵ model is based on computing eddy viscosity using turbulence kinetic energy k and turbulence dissipation rate ϵ. It represented by the following equation:

$$\nu_t = C_\mu \frac{k^2}{\epsilon} \tag{2.13}$$

Each of the two turbulence scales used have a transport equation. The exact momentum equation is used to derive the turbulence kinetic energy equation, by taking the trace of Reynolds stress.

In order to improve the performance of the standard model above, a new $k-\epsilon$ model is proposed, the Realizable $k-\epsilon$ model. In this model, Reynolds stress is always positive [24]. To do so, C_μ is a variable and computed according to the following equation:

$$C_\mu = \frac{1}{A_0 + A_s U^* \frac{k}{\epsilon}} \tag{2.14}$$

where $A_0 = 4$, $U^* = \sqrt{S_{ij}S_{ij}\Omega_{ij}\Omega_{ij}}$, $A_s = \sqrt{6}\cos(\frac{1}{3}\arccos(\sqrt{6}W))$, $W = \frac{\sqrt{8}S_{ij}S_{jk}S_{ki}}{S^3}$ and the vorticity tensor $\Omega_{ij} = \frac{1}{2}(\frac{\partial u_i}{\partial x_i} - \frac{\partial u_j}{\partial x_i})$.

The third model is the Reynolds stress model. Here, the individual Reynolds stresses are calculated using differential transport equations. Then these individual stresses are used to obtain closure of Reynolds-averaged momentum equation, this avoids the use of eddy viscosity approximation. Then exact form of the Reynolds stress transport equations can be then derived.

A 3D numerical simulation of a thin film lubricated journal bearing had been conducted under the assumption of turbulent flow. The above three models were used [24]. The static pressure and the wall shear stress were found, for different L/D ratios, for the three models.

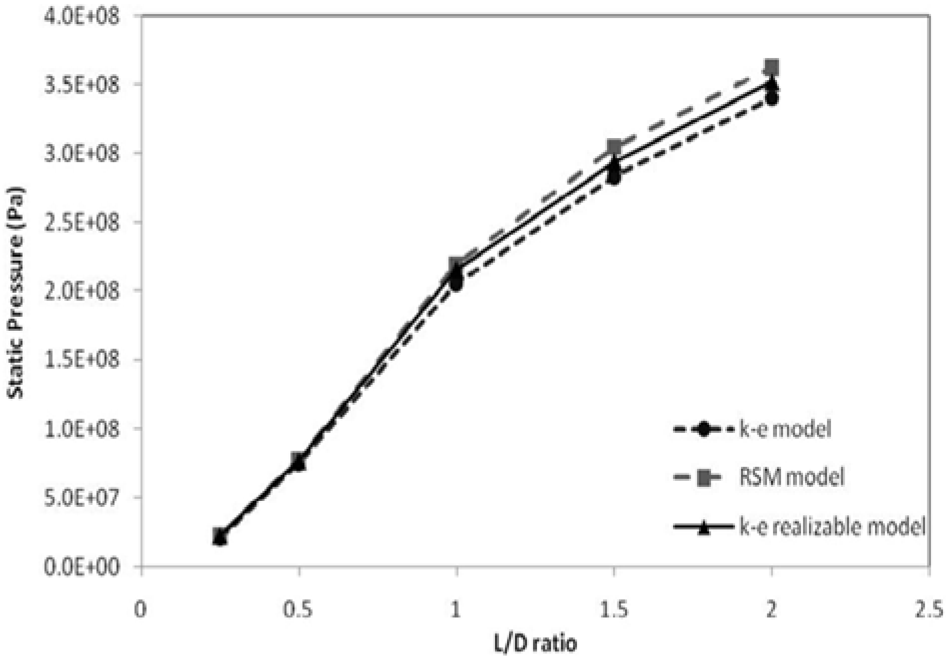

Figure 2.16: Static pressure for different L/D ratio

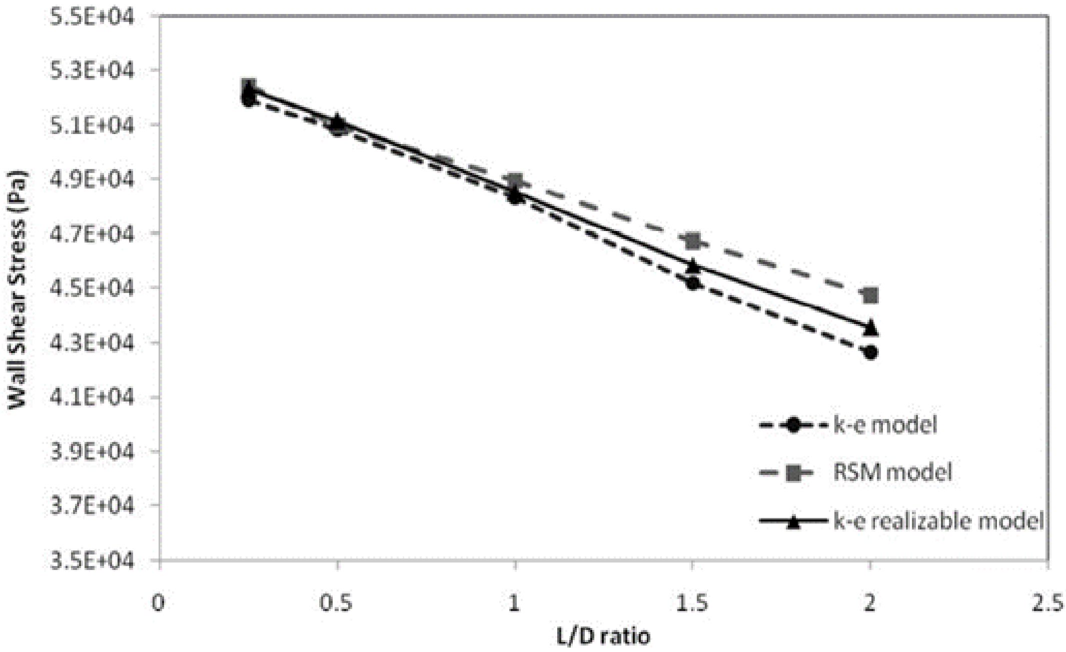

Figure 2.17: Wall shear stress for different L/D ratio

From the results in Fig 2.16 and 2.17, it is obvious that the three models are capable of modeling the turbulent flow in journal bearings simulation. The comparison shows similar results for the three models. So the standard k-ϵ model is the most suitable one because it converges faster than RSM and realizable k-ϵ and gives almost the same results.

2.5 Cavitation

The lubricating oil is considered as liquid. When the pressure decreases below fluid's vapour pressure, a new phase is formed when the change from liquid to vapour occurs, at a constant temperature. This is known as cavitation [**25** , 26]. It occurs mainly when the bearing is operated at high load or high rotational speed. The rapid change in lubricating film thickness causes the decrease of pressure because the fluid cannot fill the space immediately. Vapour pressure is then formed as a result [27]. The presence of liquid and vapour phases at the same time should be modeled by multi-phase mode. This model is expensive in terms of time and can be replaced by the mixture model. The mixture model has almost the same performance as the multi-phase model with lower computational time. The equations to be solved in this model are the continuity and momentum equations of the mixture, as well as the volume of fraction equation of the vapour-phase. Also the mass transfer between the different phases should be modeled. Vapour cavitation is modeled by the Rayleigh-Plesset model [6]. The model describes the effect of vaporization and condensation. The model is integrated in CFD Package ANSYS CFX. The change of phase is given by the difference between the rate of vaporization and the rate of condensation.

The rate of vaporization:

$$\dot{R}_{vap} = F_{vap}\frac{3r_{nuc}(1-r_V)\rho_V}{R_B}\sqrt{\frac{2}{3}\frac{\mid P_{vap}-p\mid}{\rho_l}} \tag{2.15}$$

The rate of condensation:

$$\dot{R}_{cond} = F_{cond}\frac{3r_V\rho_V}{R_B}\sqrt{\frac{2}{3}\frac{\mid P_{vap}-p\mid}{\rho_l}} \tag{2.16}$$

The source term, representing the phase change:

$$\dot{S}_v = \pm(\dot{R}_{vap} - \dot{R}_{cond}) \tag{2.17}$$

F_{vap} and F_{cond} are empirical factors, r_{nuc} is the volume of fraction of the nucleation sites, r_V is the volume of fraction of the vapour phase, ρ_V is the density of the vapour phase, P is the overall pressure and ρ_l is the density of the surrounding

liquid.
As the pressure remains below the equilibrium pressure, gas bubbles grow up. They are absorbed back to the liquid as the pressure rise up again above the equilibrium pressure. By this, Gaseous cavitation is formed, and the dissolved air is set to be free. The gaseous cavitation is described by full-cavitation model. The phase change is given by difference between the mass transfer by absorption and by desorption.

Mass transfer by absorption:

$$\dot{R}_{abs} = C_{abs}\rho_g(p_g - p_{equil})(f_{g,l,lim} - f_{g,l})f_{g,g} \tag{2.18}$$

Mass transfer by desorption:

$$\dot{R}_{des} = C_{des}\rho_g(p_{equil} - p_g)(1 - f_{g,g})f_{g,1} \tag{2.19}$$

The source term, representing the phase change:

$$\dot{S}_{da} = \dot{R}_{abs} - \dot{R}_{des} \tag{2.20}$$

C_{abs} and C_{des} are empirical factors for absorption and desorption and $f_{g,l,lim}$ is the maximal solubility of the gas in the liquid.

So the mass fraction of the gas is the sum of the free gas and dissolved gas mass fractions:

$$f_g = f_{g,g} + f_{g,1} \tag{2.21}$$

The effect of cavitation in modeling and simulating journal bearings is studied in [8]. The cavitation is neglected in one case and modeled in another one, for the same journal bearing and same boundary conditions. The results are shown in Fig 2.18.

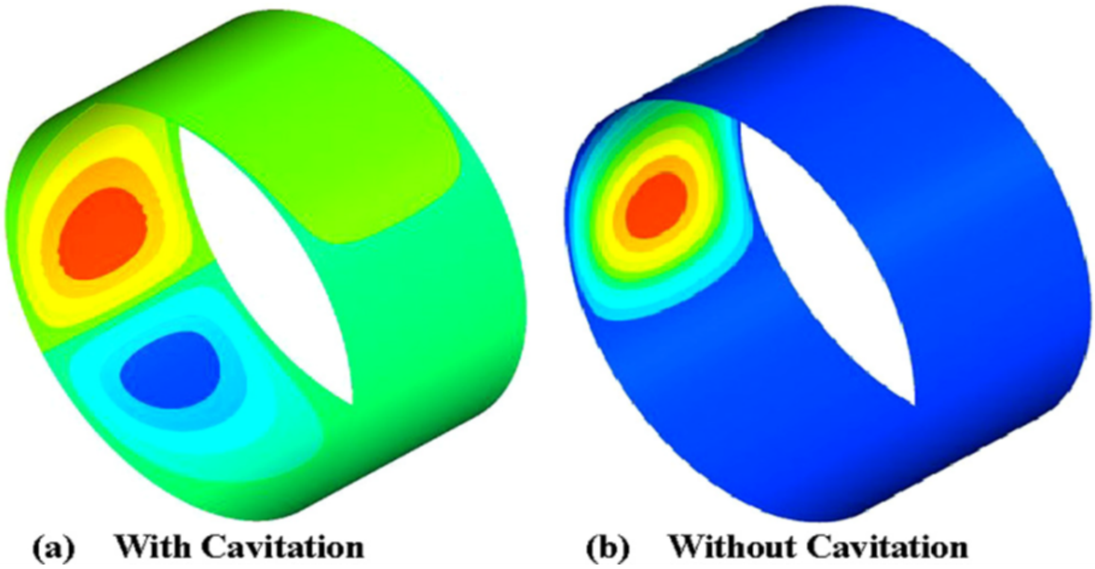

Figure 2.18: Pressure contours generated for journal bearing

There is a significant difference in the pressure contours for both cases. Due to cavitation, the pressure distribution is changed to pressure build up, and the pressure drop disappears.

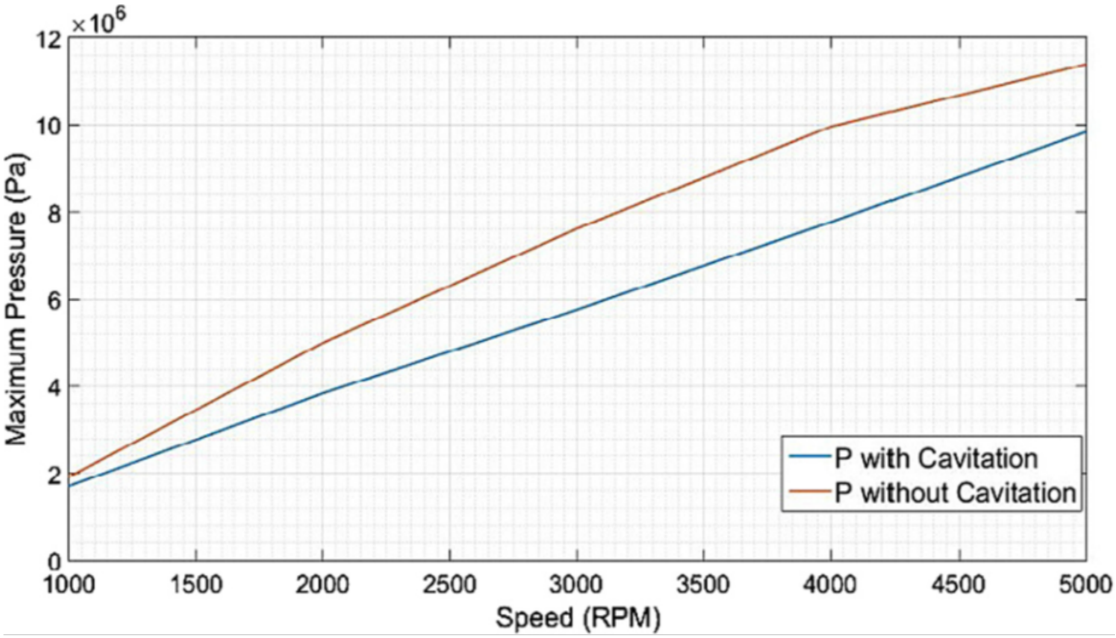

Figure 2.19: Comparison of maximum pressures in journal bearing with and without cavitation

Fig. 2.19 shows the maximum pressure for the two cases as function of the shaft rotational speed. We see that the increase in the maximum pressure have the same manner for both cases, with and without cavitation. Whereas, the maximum pressure is lower when modeling cavitation compared to the other case for each rotational speed value.

2.6 Non-Newtonian Fluids

Newtonian fluids obey Newton's law of viscosity. The viscosity is independent of the shear rate [28]. The assumption of Newtonian fluid is used in most numerical simulations of journal bearings. Whereas,in some severe cases, the real non-Newtonian behavior of the fluid is modeled [29, 30, 31, 32]. In these cases, the fluid's viscosity is not independent of the shear stress, so some parameters should be used to describe the mechanical behavior of the fluid. For this purpose, four different models are presented. The first two correspond to Pseudo plastic fluids, and the other two are refer to visco-plastic oils [28, 29, 30].
Power law Ostwald Model: For some range of shear rate, the viscosity can be represented as a power law, with the equation:

$$\mu = \mu_0 \dot{\gamma}^{n-1} \tag{2.22}$$

For n=1, the fluid is Newtonian, and n < 1 corresponds to shear-thinning fluids (non-Newtonian). This model is simple and can be used for fluids such as rubber, polymers, adhesive. The effect of temperature change can be added, and the equation becomes:

$$\mu = \mu_0 \dot{\gamma}^{n-1} \exp^{eT} \tag{2.23}$$

Carreau model: This model is an extension of the power law model. Five parameters are involved in the equation:

$$\frac{\mu \mu_\infty}{\mu_0 - \mu_\infty} = (1 + (\lambda\gamma)^a)^{n-1/a} \tag{2.24}$$

μ_0 is the zero shear viscosity, μ_∞ is the viscosity at infinite shear, λ is time constant, n is an exponent of power law, and a is a parameter describing the transition between the first Newtonian plateau and the power law zone.

Bingham model: The equation of viscosity in the presence of simple relation between shear and strain:

$$\mu = \frac{\tau_0}{\dot{\gamma}} + \mu_0 \tag{2.25}$$

τ_0 is the yield stress and μ_0 is reference viscosity.

Herschel-Bulkley Model: Used when the strain experienced by the fluid is related in a complex way to the stress. The equation is:

$$\mu = K\dot{\gamma}^{n-1} + \frac{\tau_0}{\dot{\gamma}} \tag{2.26}$$

K is the consistency index.
Modeling fluid as non-Newtonian is very important for many cases of numerical simulations, and it gives more accurate results. Whereas, in the case of hydrodynamic journal bearings, the assumption of Newtonian fluid is valid, and it simplifies the model, saves time and gives almost the same results as considering non-Newtonian fluids.

2.7 Simulation Models

Different types of modeling the journal bearings are used in numerical simulations. Depending on the working environment and the level of complexity and accuracy needed in the simulation, there are mainly four models:

Hydrodynamic (HD) Model: The model uses full Navier-Stokes equations to find the numerical solution as oil pressure distribution, film thickness, maximum pressure and load carrying capacity of the bearing. This model is the simplest one. The viscosity in the numerical simulations is considered to be constant, therefore it does not change throughout the geometry due to pressure and temperature effects. The main advantage behind using this model is the lower computational time needed for the solution to converge..

Thermo-hydrodynamic (THD) Model: In this model, the viscosity in not constant, and it changes as a result of change in the temperature [**33** , 34]. In addition to Navier-Stokes equation, energy equation is solved by taking into account the effect of the heat convection. The main difference between this model and the simple hydrodynamic model is the variability of viscosity. This leads to more accurate results, but also more computational time.

Elasto-hydrodynamic (EHD) Model: In this model, the shaft and/or the bearing are considered as deformable bodies. The elastic deformations are not neglected in this model, as compared to the first two models. The loads acting on the solid materials lead to small mechanical elastic deformations [**35** , **36** , 37]. For this model, the deformations are calculated for each time step and each node. therefore, FEM (finite element method) is used in order to find the elastic deformations [38]. Then the exchange of information occurs between the two solvers. These information are the fluid forces (pressure) and the elastic deformations. The solvers work by finding the pressure distribution first, and then stresses and deformations are evaluated using the computed pressure field. These deformations have a direct effect on the pressure, so the pressure distribution is calculated again by considering the effect of deformations.

Thermo-elasto-hydrodynamic (TEHD) Model: The most complex and time consuming model. Both elastic and thermal effects are considered in this model. The results obtained are the most accurate compared to the other three models [**40** , **41** , 39, 42, 43].

Chapter 3

Numerical Methods

3.1 Computational Fluid Dynamics CFD

In CFD applications, the equations stated earlier, Navier-Stokes equations, momentum and continuity equations, are applicable to all kind of fluids and flows. These equations are solved according to the fluid model which give a set of partial differential equations. These PDE are called the governing equations. In Fluent, the geometry is drawn using ANSYS DesignModeler. For the journal bearing, the fluid film is considered only, without taking into account the solid material. The geometry appears in Fig 3.1.

In order to solve the set of PDE for the entire model, ANSYS uses discretization methods. Finite volume method is one of these methods used to solve the numerical problem. The computational domain is divided into smaller regions or parts. These are called the cells or the control volumes. In ANSYS, these cells form the called "mesh". Fluent uses finite volumes to transform the general equations into algebraic equations, which will be solved by CFD solver using some iterative methods. The working algorithm of CFD solver is presented in Fig 3.2.

The mesh is created using mesh sizing and face meshing, see Fig. 3.3. Tetrahedral cells are formed, with total number varying between one to one and half million cells according to different cases.

After creating the mesh, the model should be defined in the Fluent set up. Transient mode is selected, and gravity is to set $-9.81m/s^2$ in the y-direction. In the models section, multiphase is kept off since we are not considering the effect of cavitation, so only one phase is present, which is the liquid phase. The energy equation is on, because viscosity is dependent of temperature variation. Flow is assumed to be laminar. The lubricant used has the following properties: density =

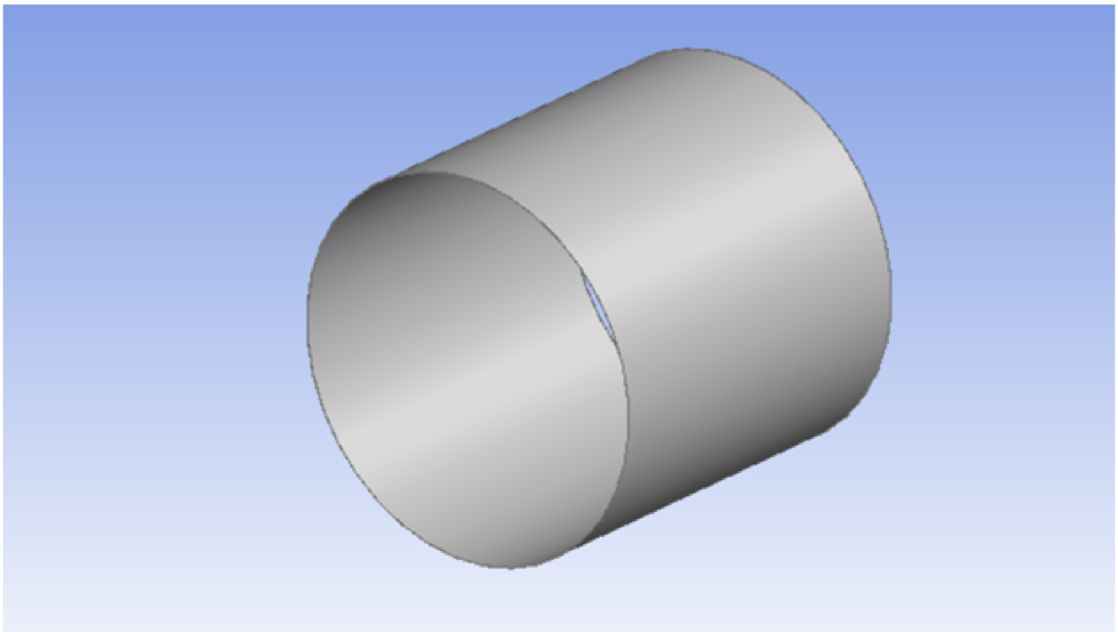

Figure 3.1: Journal Bearing Geometry

850 kg/mm^3; specific heat = $2000J/kg°C$; Thermal conductivity = $0.13W/m°C$ and lubricant viscosity = $0.04986Pa - Sec$

The fluid properties are imported to Fluent and a new fluid is created according to these values.

For the boundary conditions, the inlet and outlet are set be pressure inlet and outlet with zero gauge pressure. In Fig 3.4, the blue arrows describe the inlet, and red arrows are related to the outlet of the domain. The outer wall is fixed, because it is in contact with the fixed bearing element. While the inner wall is set to be moving in a rotational manner according to the rotational speed of the shaft.

The CFD solver finds an initial solution for the model variables using standard or hybrid initialization. In the standard initialization, the initial values in terms pressure, velocity and temperature, should be manually added, while for hybrid initialization, the solver uses some iterations to find an initial solution of the system. The initial solution should be accurate with tolerance less than 10^{-6}.

In the solution methods, SIMPLE or PISO method could be used for pressure-velocity coupling. As for the spatial discretization, Least Squares Cell Based used for gradient, Second Order used for pressure, and First Order Upwind for both momentum and energy. The time step used is 0.1 seconds. The number of time steps is 10 with 5 maximum iterations for each time step.

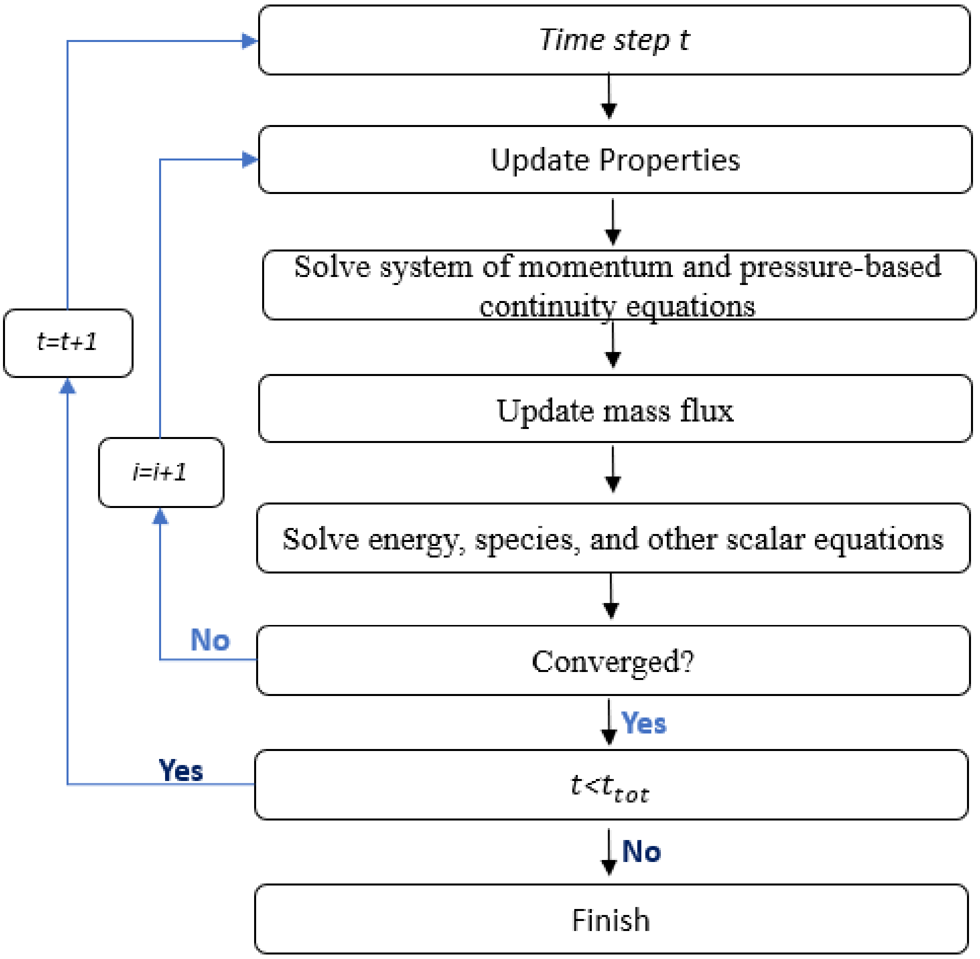

Figure 3.2: CFD working algorithm

3.2 Finite Element Method FEM

To study the dynamic behavior of the solid material (bearing and journal), the equation of motion (3.1) should be solved.

$$m\ddot{u} + c\dot{u} + ku = p(t) \tag{3.1}$$

m is the structural mass matrix, c is the structural damping matrix, k is the structural stiffness matrix and u is the displacement vector.
In ANSYS, using transient structural, this equation should be solved to find the

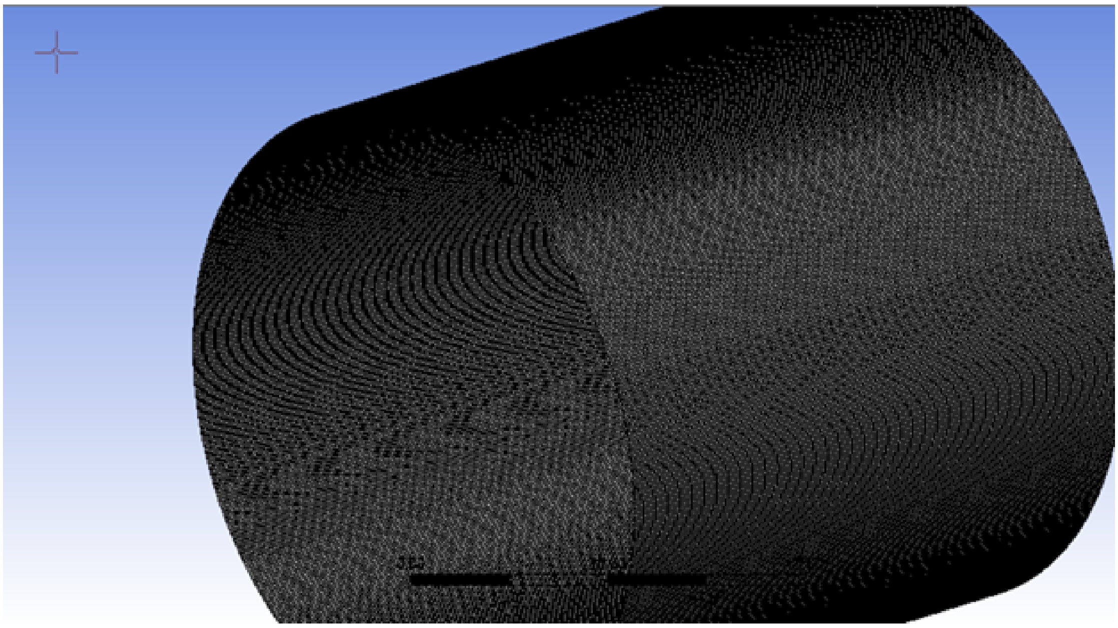

Figure 3.3: Journal Bearing Mesh

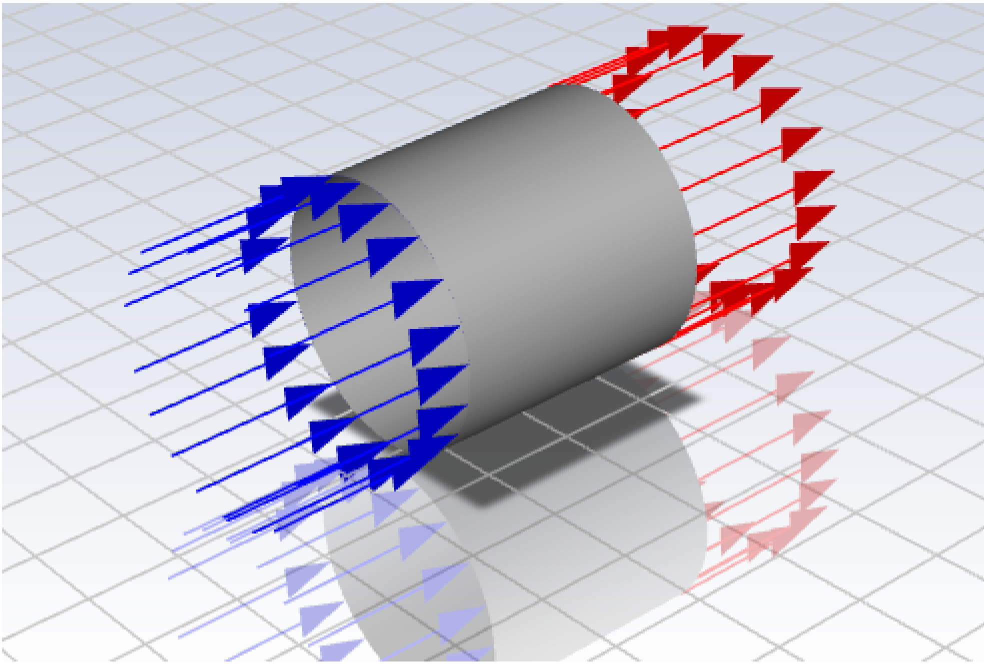

Figure 3.4: Journal Bearing Setup

displacement, stress and stress in the domain of study. The damping is not covered by transient structural, so the equation is simplified into:

$$m\ddot{u} + ku = p(t) \tag{3.2}$$

In this equation, the number of degrees of freedoms DOFs is infinite. The equation cannot be solved by analytical methods. The working principle behind the numerical method is to divide the volume of the structure into smaller elements, by which the infinite DOFs transformed into finite number of freedoms with finite number of equations that are solved to find the required results.

in order to solve the equation of motion, the numerical system performs several steps. First, a system of finite elements is formed, in which these finite elements are interconnected at the formed nodes. At these nodes, the DOFs are defined. For each element, the elements of the stiffness and mass matrices and of the force vector are determined. The equations relating the force, displacement and acceleration are:

$$f_{s,e} = k_e u_e \tag{3.3}$$

$$f_{I,e} = m_e \ddot{u}_e \tag{3.4}$$

where $f_{s,e}$ is the force element, $f_(I, e)$ the inertial force element, k_e is the element of stiffness matrix, m_e is the element of mass matrix, u_e and $\ddot{u}_e$ are the displacement and acceleration vectors related to the element.

The elements of k_e, m_e and u_e are used to create a global matrices. The elemental displacements are related to the global matrix u by:

$$u_e = a_e u \tag{3.5}$$

The global stiffness and mass matrices, in addition to the force vector are formed by

$$k = A_{e=1}^{N} k_e \tag{3.6}$$

$$m = A_{e=1}^{N} m_e \tag{3.7}$$

$$p(t) = A_{e=1}^{N} p_e(t) \tag{3.8}$$

where $A_{e=1}^{N}$ is an assembling operator. Then the final equation of motion is created. By using some iterative methods, the equation can be solved to find the values of $u(t)$.

In ANSYS Transient Structural, the geometry is drawn showing the whole system as shown in Fig. 3.5, which includes the bearing, journal and the clearance between them.

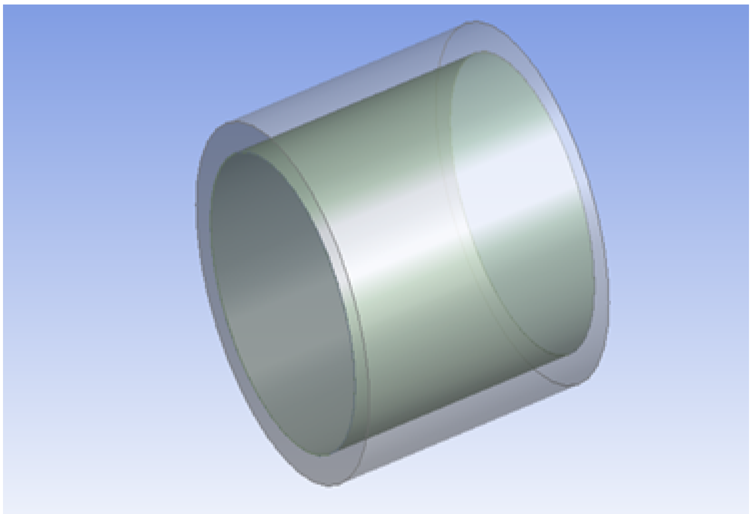

Figure 3.5: Goemetry of the Journal Bearing System

After drawing the geometry, discretization is formed using meshing, as shown in the Fig. 3.6.

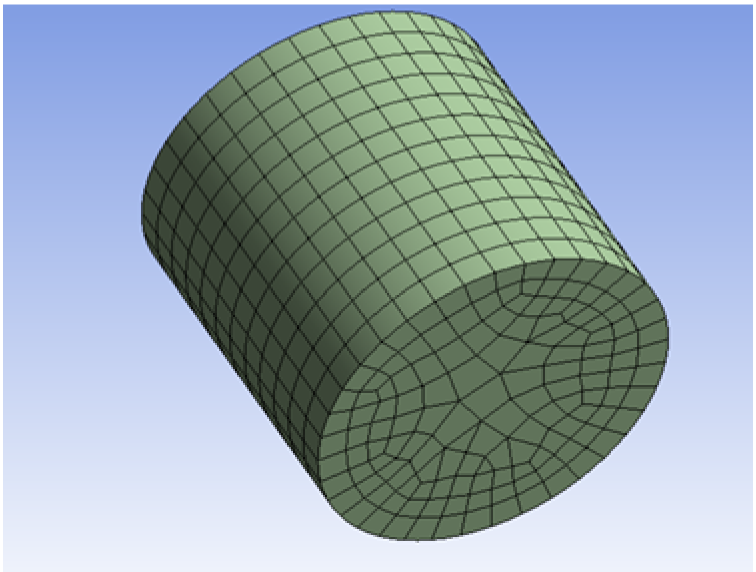

Figure 3.6: Discretization of the shaft and the bearing

When working on the system setup, the outer surface of the bearing is constraint by cylindrical support. The load acting on the inner surface of the bearing and the outer surface of the journal is coming from the fluid pressure. This pressure is imported by coupling Transient Structural with Fluent. Then the system is solved for this load as an input to find the elastic deformations at each node.

3.3 System Coupling

The fluid structure interaction FSI is done by modeling both systems together. Fluent and transient structural are coupled together by System Coupling. System coupling enables the exchange information and results between the two systems. The system coupling receives the information from both systems and sends the required information for them of to complete the solution procedure.

There are two kinds of coupling, one way coupling and two ways coupling. The later is the one used in this thesis. The one way coupling works by sending the converged solution at each time step from Fluent to ANSYS MECHANICAL (transient structural), which uses this solution in its solving procedure. On the other hand, two ways coupling enables the exchange of information between the two systems. Fluent finds the pressure values and send them to ANSYS MECHANICAL. It uses these results to evaluate the displacement. Then it sends back the results to the Fluent. Fig. 3.7 summarizes the working principle of the FSI system, and shows the exchange of information between the two solvers.

In ANSYS, the two way coupling is completed as shown in Fig 3.8
The working principle is summarized in the following steps:

1. The geometry is imported in the ANSYS Design Modeler.
2. ANSYS Engineering Data used to set the material properties for the shaft and bearing.
3. The geometry is passed off to the Transient Structural.
4. Mesh is created in both systems.
5. Fluid creation and initialization is done in Fluent.
6. Transient Structural set up is initialized.
7. System Coupling is initialized. Fluid Structure Interface is created between the outer surface of the lubricating oil and the inner surface of the bearing. Another Fluid Structure Interface is created between the inner surface of the lubricating oil and the outer surface of the journal. These two FSI stand for the Data transfer between the two systems.

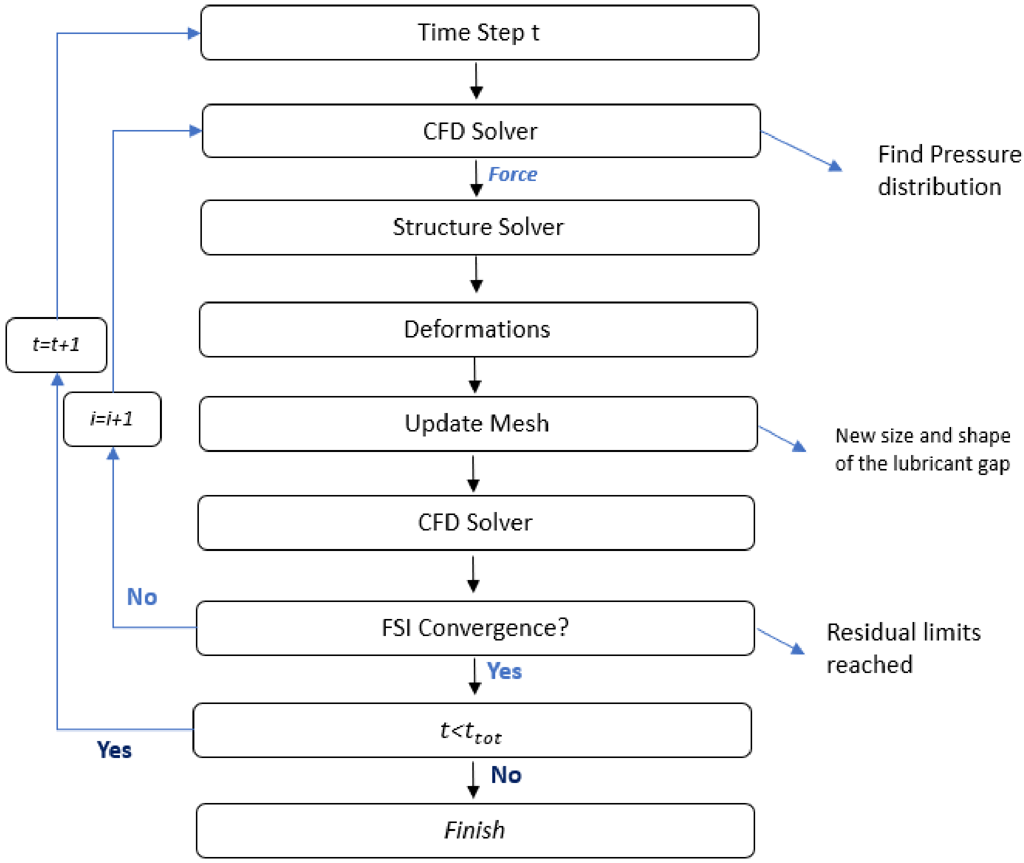

Figure 3.7: System Coupling Algorithm

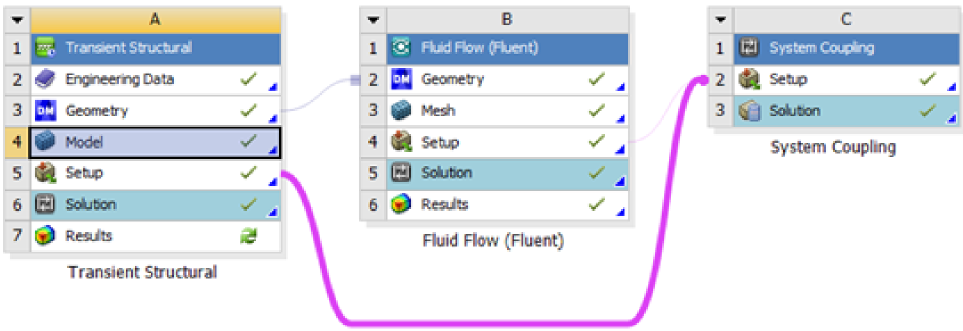

Figure 3.8: ANSYS System Coupling

8. The first iteration of FSI cycle:
   (a) Converged cycle is completed in Fluent.
   (b) Forces acting on the bearing/shaft are transformed into Transient Structural through System Coupling, and recorded in ANSYS Post CFD.
   (c) Transient Structural solves the displacement, and the results transformed into Fluent where new converged cycle is solved.
   (d) This cycle stops only when the final time setup is reached.
   (e) Converged solution of the FSI system is reached when the two systems reached their residual limit (10^{-6}). In this case, the value of pressure at the node is compatible with the deformation values for the same node.

The same procedure is carried for both fluent and mechanical parts as if they are separate components. While some different steps should be considered: In Fluent, dynamic mesh should be used. This is necessary because of the effect of deformations on the fluent mesh. Fluent should be solved using coupled solution rather than simple or PISO. The fluid outer face is coupled with the bearing inner face, and the fluid inner face is coupled with the shaft outer face. The number of time steps (10) and the step size ($0.1s$) are set in the coupled analysis. These values should be compatible with the values in the two subsystems.

Chapter 4

Results and Discussion

The shaft and the bearing are made of steel. The lubricating oil has the following properties: density = 850 kg/mm^3; specific heat = 2000 $J/kg°C$; Thermal conductivity = $0.13 W/m°C$ and lubricant viscosity = $0.04986 Pa - Sec$ (see table 4.1). The shaft diameter=100 mm; the bearing diameter=140 mm and the radial clearance is 0.1 mm. The attitude angle is set as 55° for all considered case (see table 4.2.

Density (kg/mm^3)	Specific Heat ($J/kg°C$)	Thermal Condutivity ($W/m°C$)	Viscosity ($Pa - Sec$)
850	2000	0.13	0.04986

Table 4.1: Properties of the used lubricant oil

Outer Diameter (mm)	Inner Diameter (mm)	Radial Clearance (mm)	Attitude Angle (°)
140	100	0.1	55

Table 4.2: Geometric Dimensions of the Model

The eccentricity ratio is set to 0.6, and the shaft rotates with a rotational speed of 2500 rpm. These values are used in the numerical procedure to find the pressure distribution both with FSI (coupled solution) and without FSI (only Fluent). In the FSI model, the shaft and the bearing are modeled as deformable bodies, whereas in non FSI model, they are modeled as rigid bodies. Then for both coupled and

Fluent cases, the rotational speed is changed from 2500 to 3500 to 5000 rpm, in order to study the effect of changing the shaft rotating speed on the final results. Then the eccentricity ratio effect on the oil pressure distribution is also examined. This study is completed by keeping the rotational speed constant at 2500 rpm, and changing the eccentricity ratio from 0.6 to 0.7 then to 0.8 for both cases (rigid and deformable bodies).

4.1 Fluent FSI comparison

After running the ANSYS simulations for both rigid and deformable cases for 2500 rpm and 0.6 eccentricity, the results in terms of oil pressure distribution are presented in Fig. 4.1 and 4.2.

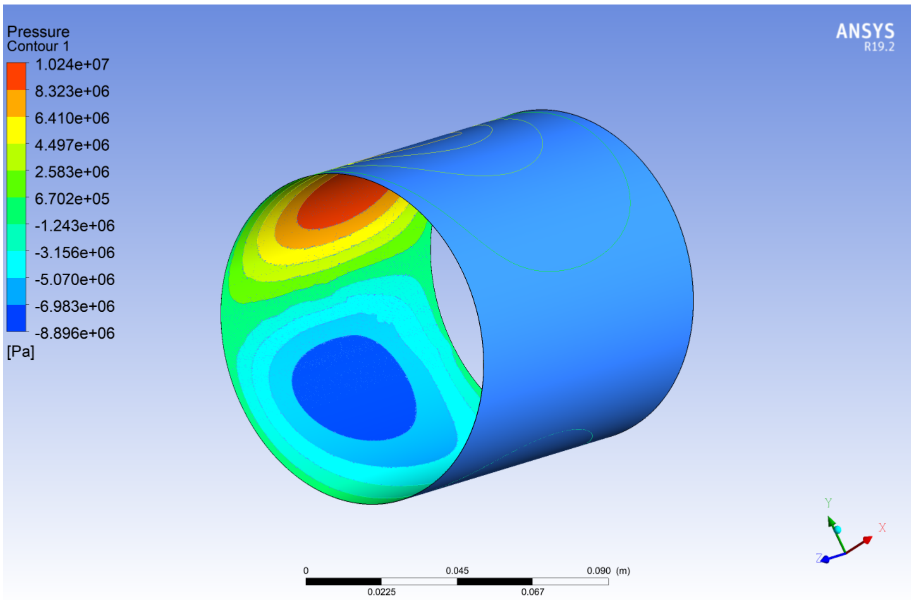

Figure 4.1: Oil pressure distribution for rigid component at 2500 rpm and 0.6 eccentricity ratio

The oil pressure distribution in both cases has the same shape. The areas for maximum pressure and minimum pressure are similar. The major difference appears in the values of the maximum pressure. We can see that the maximum pressure found by running Fluent only is 10.24 MPa (Fig. 4.1), where the elastic deformations effect are not considered. Whereas in the case where the system is solved by system coupling, using CFD and Mechanical solvers, the value of the maximum pressure is 10.8% less compared to Fluent result, and the value was found to be 9.241 MPa (Fig. 4.2).

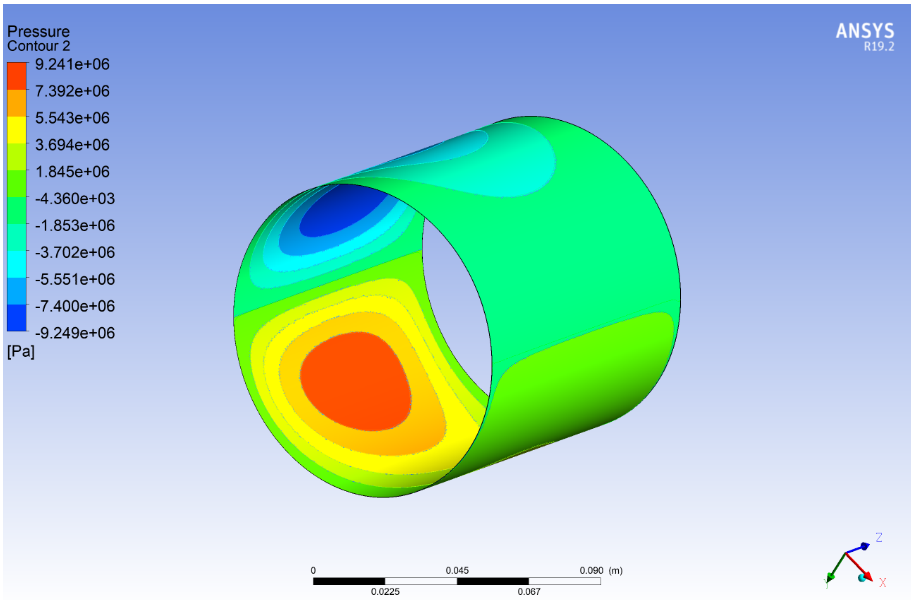

Figure 4.2: Oil pressure distribution for deformable components at 2500 rpm and 0.6 eccentricity ratio

The difference in the maximum pressure values is justified by the effect of elastic deformations of the shaft and the bearing. The elastic deformations presented in Fig 4.3 causes a change in the actual geometry of the lubricant gap. This change in geometry has a direct effect on the pressure created inside the gap.

The numerical system works by sending the values of pressure created in Fluent system to the mechanical system as load inputs. These inputs are the source of the elastic deformations, these deformations cause the decrease in the maximum presssure inside the lubricant gap. The final results obtained are more realistic since they better describe the system performance.

By modeling the elastic deformations inside the system, the maximum pressure is more accurate and has lower value than the case with rigid components. The cost for obtaining the more accurate results is paid as a larger computational time. The system needs 20 to 30 minutes to obtain the final solution in the case of rigid bodies; whereas the computational time varies between 16 to 20 hours for completing the solution for the FSI system. This is justified because there is a coupled analysis in which two solvers are working together and they exchange information between each other at each iteration.

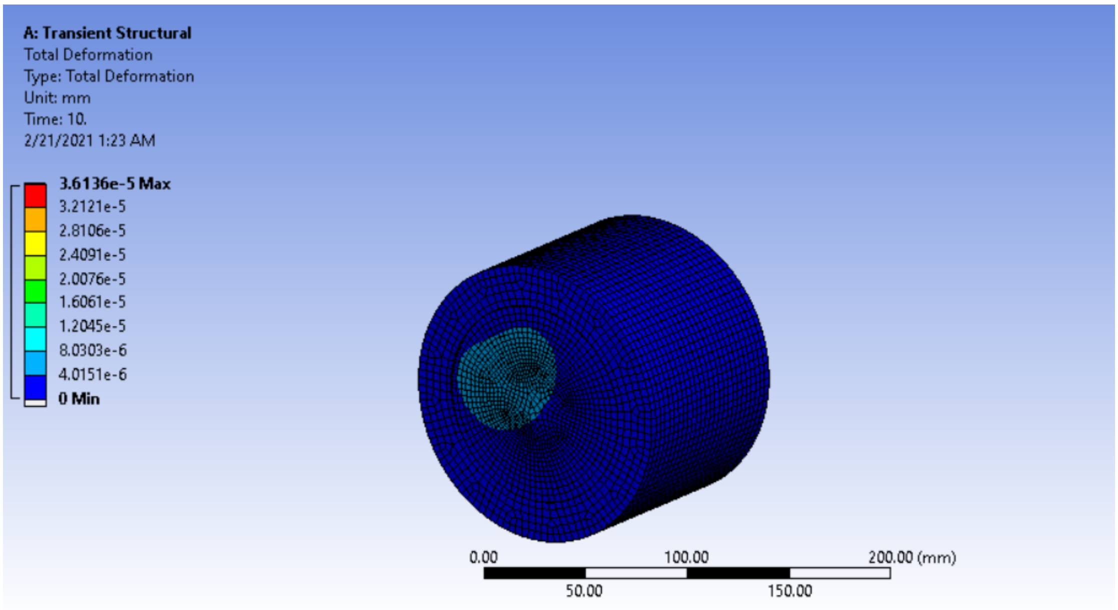

Figure 4.3: Elastic deformations of the Journal Bearing and the Shaft at 2500 rpm and 0.6 eccentricity ratio

4.2 Changing of shaft rotational speed

Changing the rotational speed of the shaft will change the pressure created inside the lubricant gap. When we increase the rotational speed, the pressure will increase as well because it is created by the effect of the shaft rotation. To study this effect, we changed the rotational speed of our system from 2500 to 3500 then to 5000 rpm, keeping other parameters unchanged. The study is done for both rigid and deformable cases.

For the case of rigid components, we can see how the maximum pressure increased from 10.24 MPa, for 2500 rpm (Fig. 4.1), to 14.14 MPa when rpm increased to 3500 (Fig. 4.4), then the maximum pressure further increased to 19.91 MPa when the rpm increased to 5000 rpm (Fig. 4.5).

Although maximum pressure is increasing with increasing the shaft rotational speed, but the shape of the pressure profile is showing similar trend for these cases. This pressure profile keeps the same shape also for modeling deformable bodies. As we can see in Figs. 4.6 and 4.7, the values of maximum pressure when considering deformable bodies increased with increasing the shaft rotational speed, but still lower than the cases with rigid components for each rpm value. The maximum pressure is 12.94 MPa for 3500 rpm (Fig. 4.6) and 18.49 MPa (Fig. 4.7). These

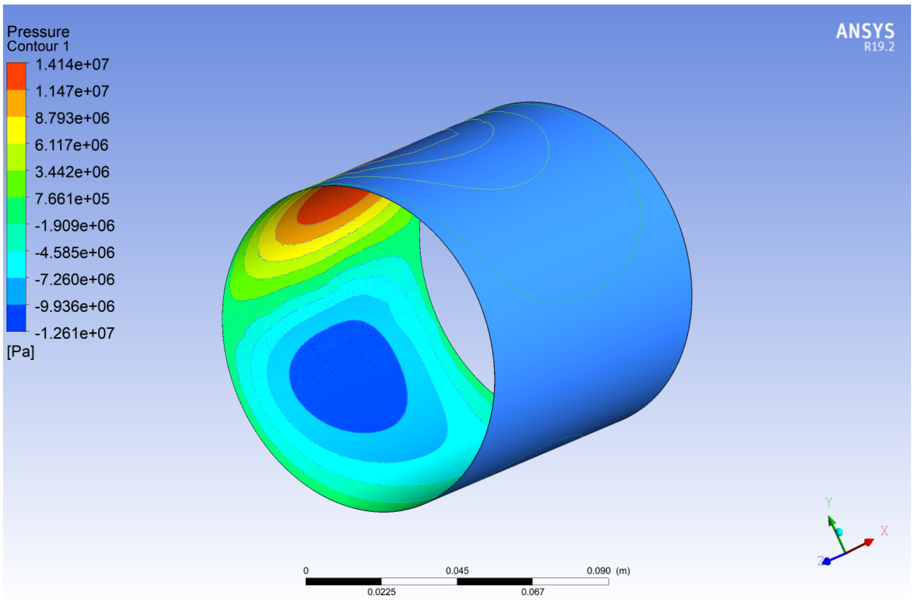

Figure 4.4: Pressure distribution for rigid component at 3500 rpm and 0.6 eccentricity ratio

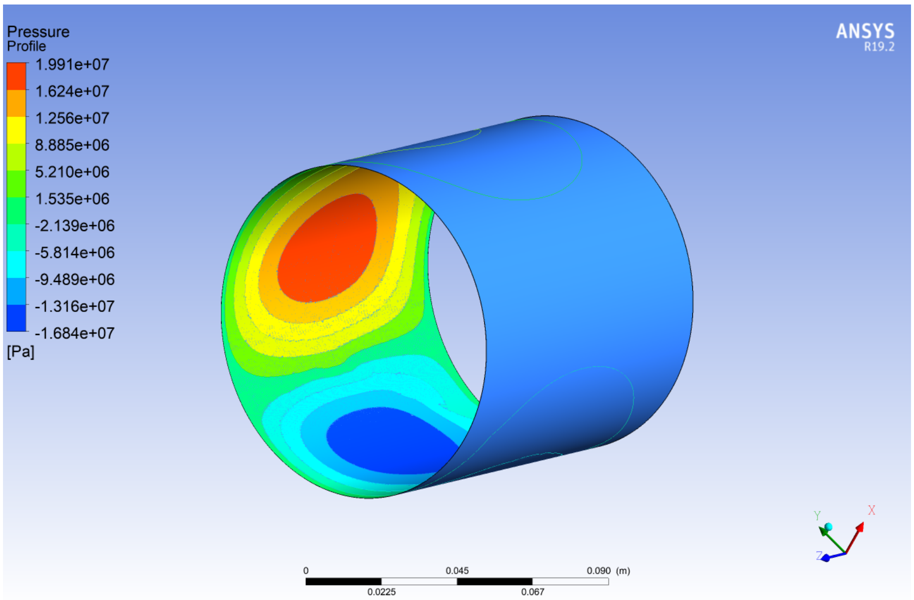

Figure 4.5: Pressure distribution for rigid component at 5000 rpm and 0.6 eccentricity ratio

values are lower than the maximum pressure values for the rigid bodies cases at 3500 and 5000 rpm respectively.

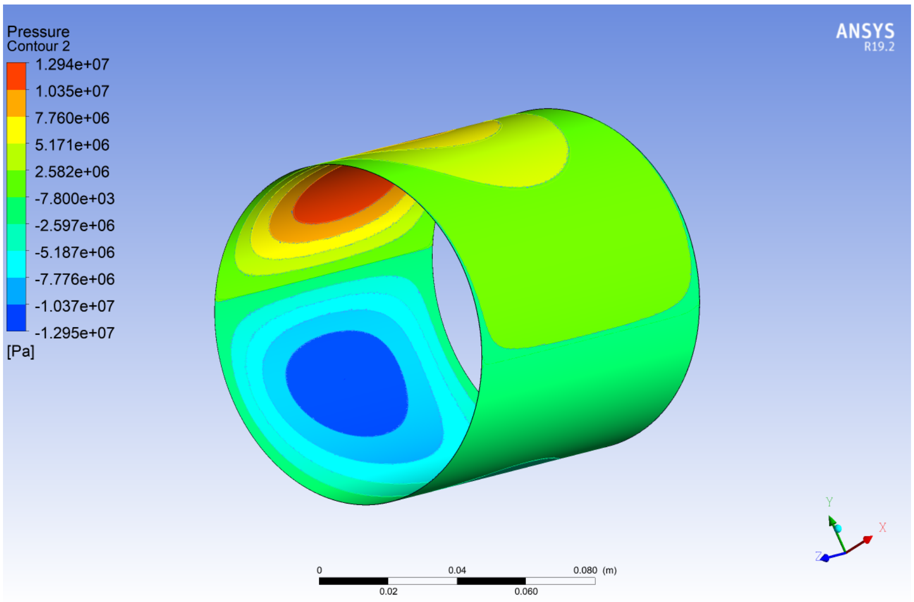

Figure 4.6: Pressure distribution for deformable component; 3500 rpm and 0.6 eccentricity

The variations of the maximum pressure for both cases (rigid and deformable) are summarized in Fig. 4.8. The results show that the difference between maximum pressure values for both rigid and deformable cases decreases from 10.8% to 7.7% as we go from 2500 to 5000 rpm. Moreover, Fig. 4.8 shows that the maximum pressure increases linearly with the increase of the shaft rotational speed.

As for the elastic deformations, the increase of the rotational speed leads to increase in the elastic deformations of the shaft and the bearing. The deformations for the 3500 rpm and 5000 rpm are shown in Fig. 4.9 and 4.10. This is justified by the increase of the input loads to the mechanical system coming from Fluent. These loads are created by the effect of pressure. The increase of pressure will cause these load to increase, and thus increase of the elastic deformations.

The increase of deformations as function of shaft rpm is shown in Fig. 4.11. The elastic deformations was 3.6136×10^{-5} mm at 2500 rpm, they increased to 5.0604×10^{-5} mm at 3500 rpm, then they increased more to 7.2317×10^{-5} mm at 5000 rpm.

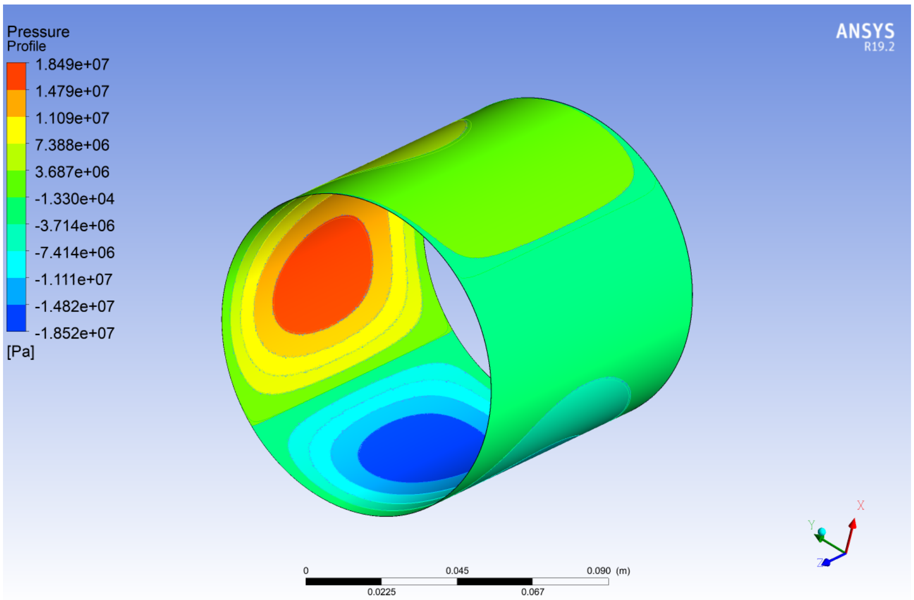

Figure 4.7: Pressure distribution for deformable component; 5000 rpm and 0.6 eccentricity

In addition to the elastic deformations, the stress and strain levels are also calculated. Table 4.3 shows the maximum stress and maximum strain experienced by the shaft and the bearing for each case, depending on the value of the rpm.

Shaft Rotational speed (rpm)	2500	3500	5000
Stress (kPa)	397.23	556.24	794.84
Strain ($10^{-5}mm/mm$)	2.9956	4.1949	5.995

Table 4.3: Stress and Strain levels for different rotational speed values

From the results shown in the table, it is clear that the stress and strain levels increase linearly with the increase of the shaft rotational speed.

4.3 Effect of changing the eccentricity value

The ratio between the distance between the centers, of the shaft and the bearing, and the radial clearance is defined as the eccentricity ratio. This geometrical parameter has a direct effect on the pressure created inside the lubricant gap. As the eccentricity ratio increases, the convergent zone will be smaller. In this case, for the same rotational speed, the volume inside the lubricant gap of the convergent zone gets smaller, so the value of the maximum pressure will increase. To investigate

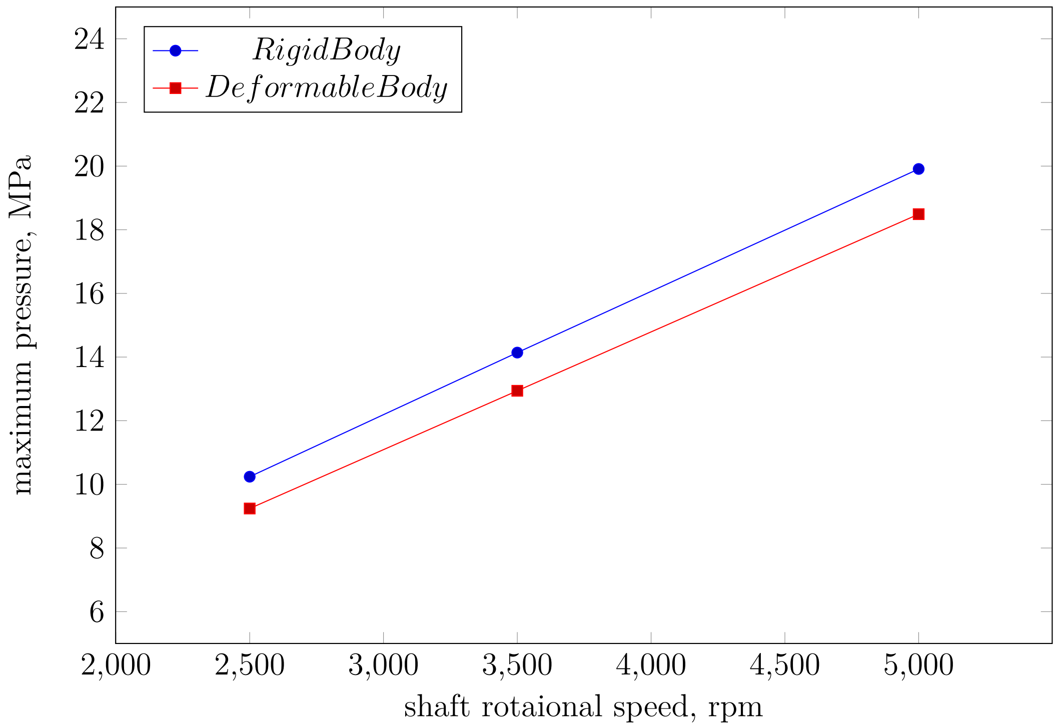

Figure 4.8: Maximum Pressure as function of shaft rotational speed

the effect of increasing the eccentricity ratio on the maximum pressure inside the lubricant gap, we increased the eccentricity ratio from 0.6 to 0.7 then to 0.8. The study is done for both cases, rigid and deformable bodies.

For the case of rigid bodies, the pressure distribution for 0.7 eccentricity value is shown in Fig. 4.12. The value of the maximum pressure is 16.20 MPa, higher than that at eccentricity ratio 0.6 (10.24 MPa). Then for eccentricity ratio of 0.8, the pressure distribution shown in Fig. 4.13 appears to have different distribution compared to other cases. The maximum and minimum pressure areas are very small compared to the cases of eccentricity ratios 0.6 and 0.7. In addition, the most important outcome is the value of the maximum pressure. We can see from 4.13 that the maximum pressure is 475.4 MPa, which is very large and not consistent with the maximum pressure values for eccentricity ratios 0.6 and 0.7. This value of the maximum pressure is not expected for the input values in the numerical model. In this case, we can check the validity of this study by looking at maximum pressure in the deformable bodies model for the same eccentricity ratio (0.8).

For the second study, considering the effect of elastic deformations, the pressure distribution obtained for eccentricity ratio 0.7 is shown in Fig. 4.14. The maximum

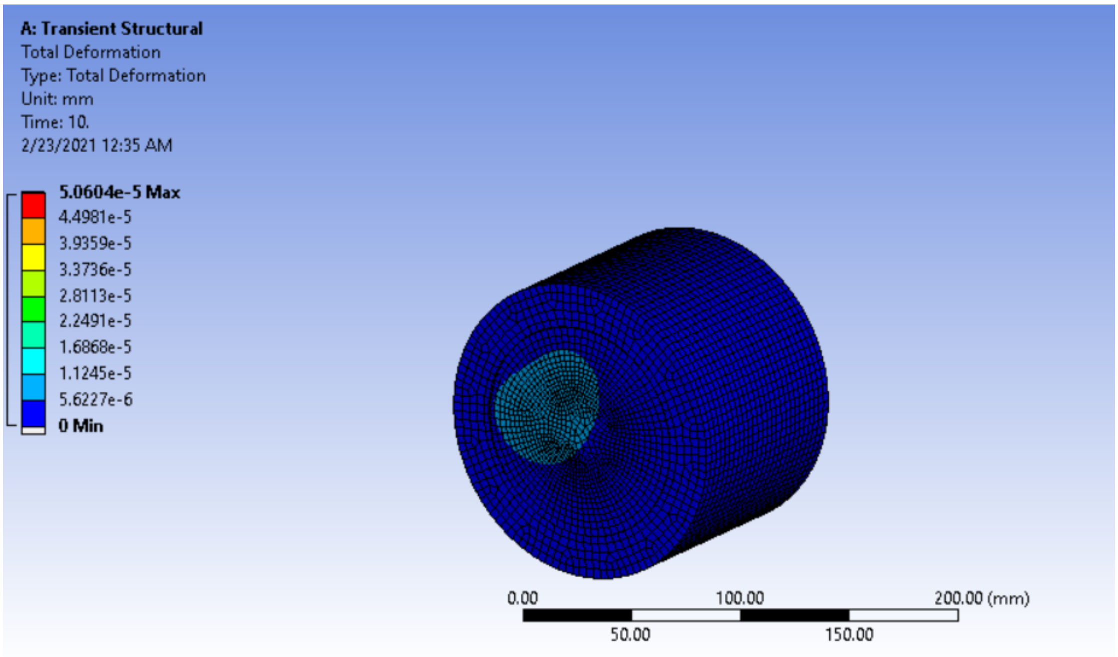

Figure 4.9: Elastic deformation for shaft and bearing at 3500 rpm and 0.6 eccentricity ratio

pressure value is 15.75 MPa, higher than that in case of 0.6 eccentricity ratio for deformed bodies case (9.241 MPa). In Fig. 4.15, the pressure distribution is shown for increasing the eccentricity ratio more to 0.8. The maximum pressure increases also in this case, and has a value of 31.35 MPa.

Considering the effect of increasing the eccentricity ratio on the elastic deformations of the shaft and the bearing, the deformations are plotted in terms of eccentricity values in Fig 4.16. The total elastic deformations increased from 3.6136×10^{-5} to 6.1312×10^{-5}, then to 11.77×10^{-5} by increasing the eccentricity ratio from 0.6 to 0.7, then to 0.8, respectively. Figs. 4.3, 4.17 and 4.18 show the elastic deformations for different eccentricity ratios at 2500 rpm.

By comparing the lubricant pressure profile at eccentricity ratio 0.8, Figs. 4.14 and 4.15, it seems that for this high eccentricity ratio (0.8), the assumption of rigid bodies is not valid, and the results are totally different from the real results. For lower eccentricity ratios, the rigid bodies model gave less accurate results by overestimating the maximum pressure values, but the results were close with a percentage of error not higher than 12%. Whereas in the case of 0.8 eccentricity ratio, the results were totally different and the CFD solver cannot give us the desired results. These results are justified by the very high levels of elastic deformations

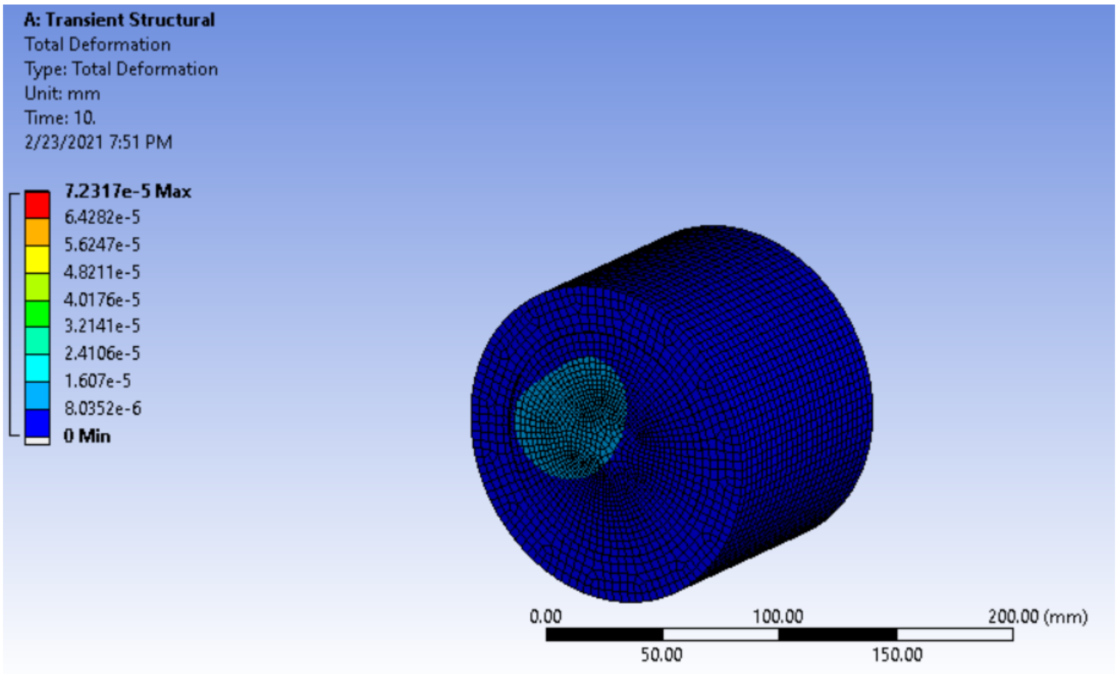

Figure 4.10: Elastic deformation for shaft and bearing at 5000 rpm and 0.6 eccentricity ratio

for high eccentricity ratios. These elastic deformations are high in this case due to the high oil pressure created inside the lubricant gap. The problem comes from the fixed lubricant gap size and shape in the rigid bodies model, because deformations are not taken into account. In this case, the pressure values will be very high compared to the real case, since the lubricant gap modeled is smaller than the real gap. Whereas, for the real case, where elastic deformations are considered, the real lubricant gap area will be modeled based on the effects of the elastic deformations. This will help the solver in finding the correct pressure distribution inside the lubricant gap.

Similar to the study of the rotational speed effect, in the previous section, the maximum stresses and strains for each eccentricity ratio are recorded in table 4.4.

Eccentricity Ratio	0.6	0.7	0.8
Stress (kPa)	397.23	679.01	1448.1
Strain ($10^{-5} mm/mm$)	2.9956	5.0773	9.7242

Table 4.4: Stress and Strain levels for different eccentricity ratios

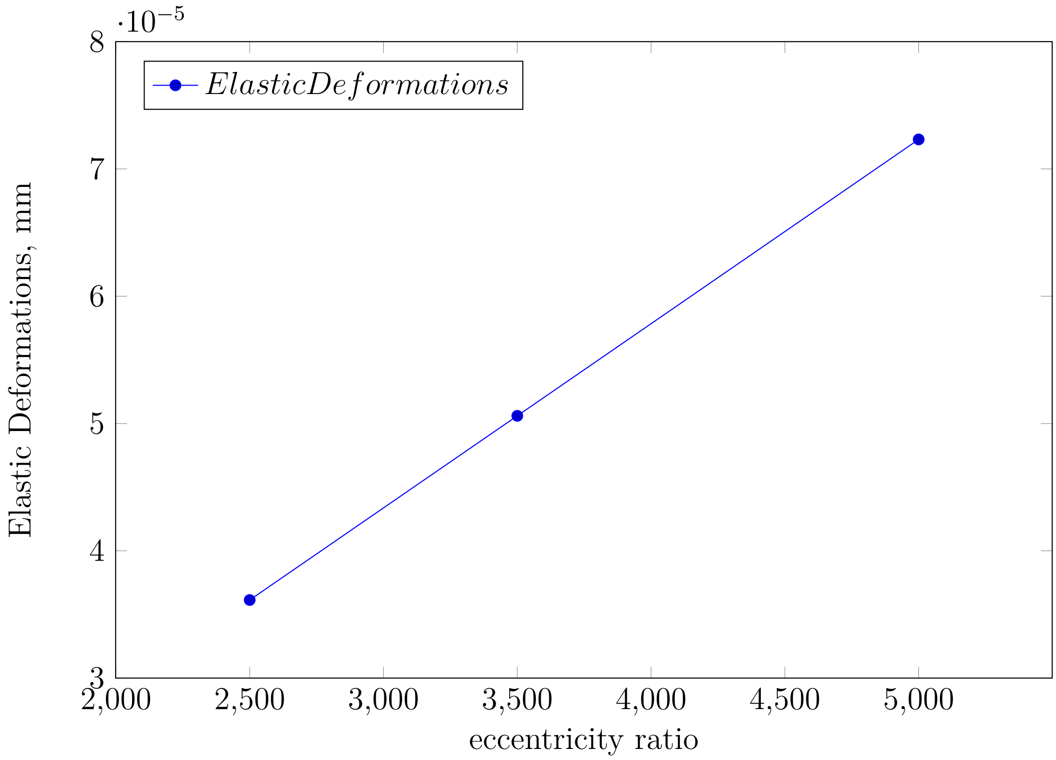

Figure 4.11: Elastic deformations as a function of eccentricity ratio

We can see the non linear increase of the maximum stress and maximum strain values as the eccentricity ratio increased from 0.6 to 0.8.

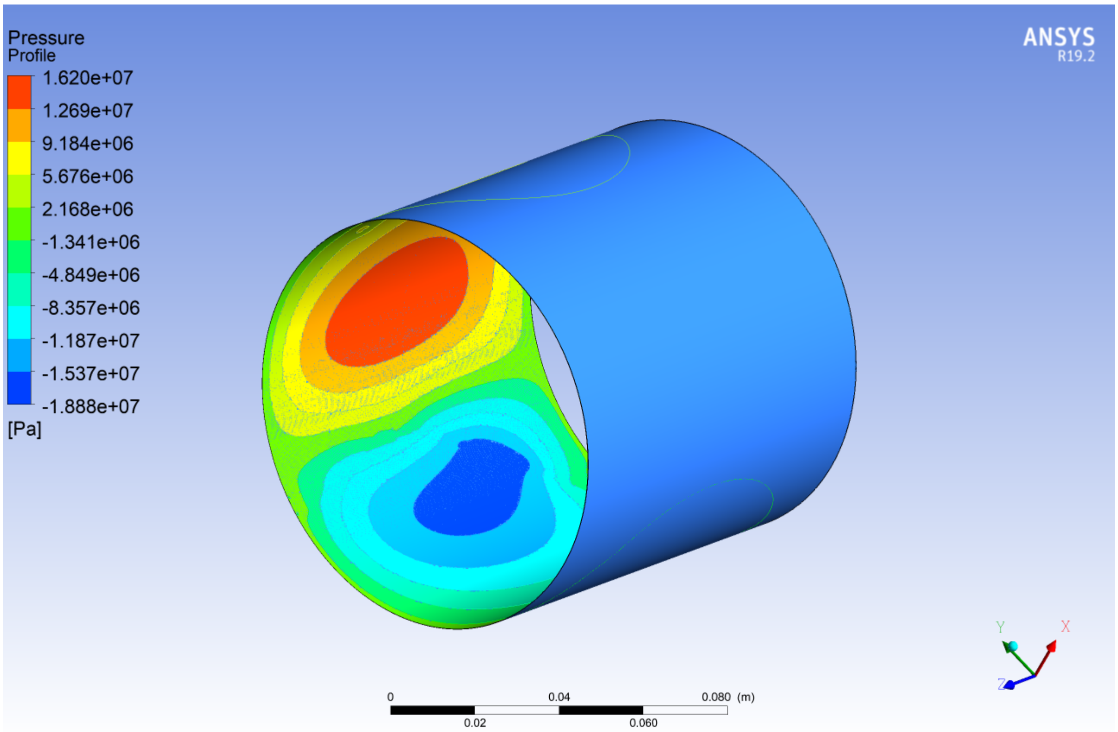

Figure 4.12: Oil pressure distribution for rigid components at 2500 rpm and 0.7 eccentricity ratio

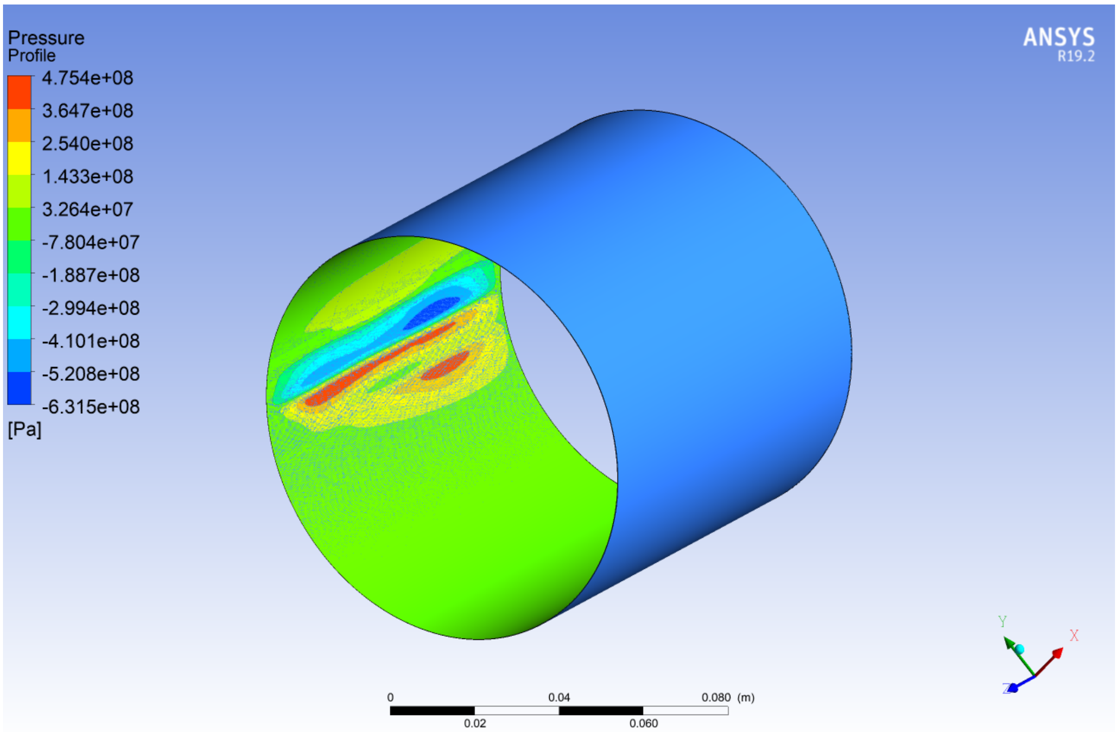

Figure 4.13: Oil pressure distribution for rigid components at 2500 rpm and 0.8 eccentricity ratio

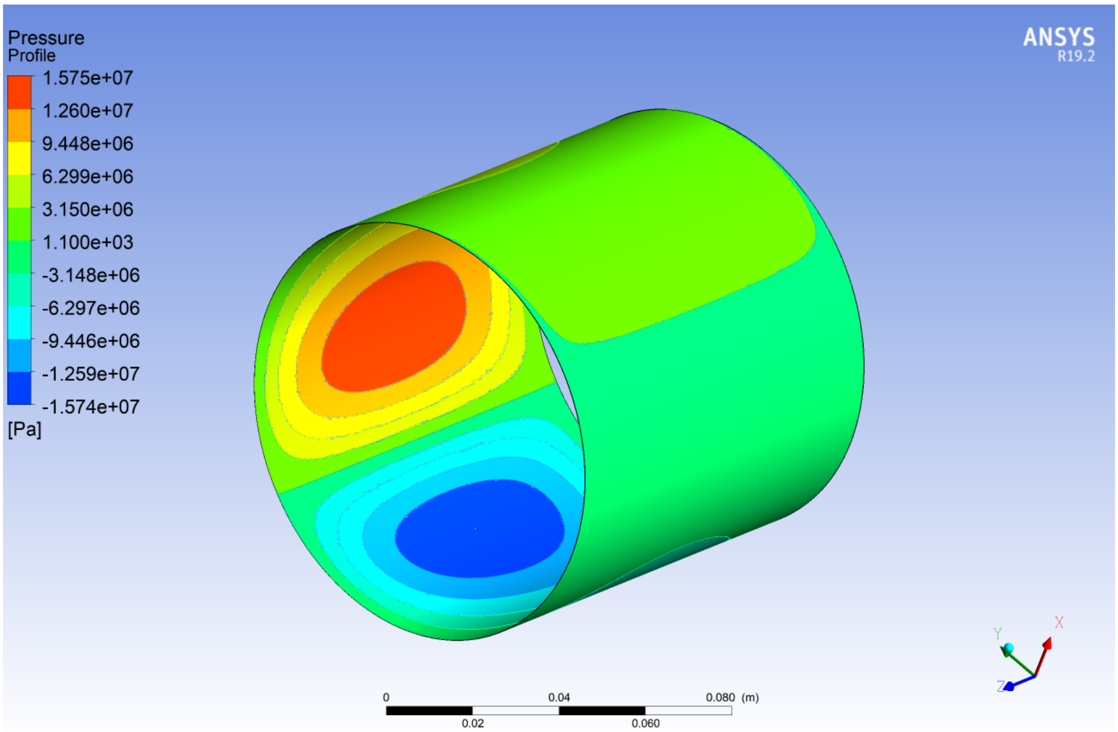

Figure 4.14: Oil pressure distribution for deformable components at 2500 rpm and 0.7 eccentricity ratio

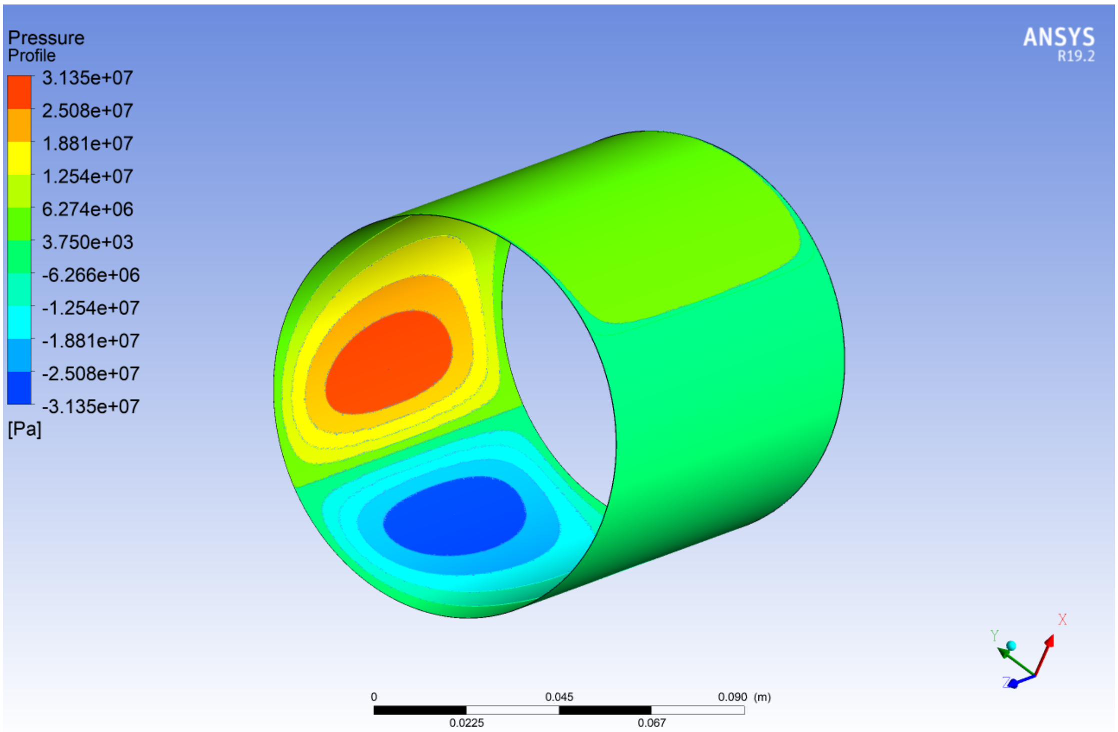

Figure 4.15: Oil pressure distribution for deformable components at 2500 rpm and 0.8 eccentricity ratio

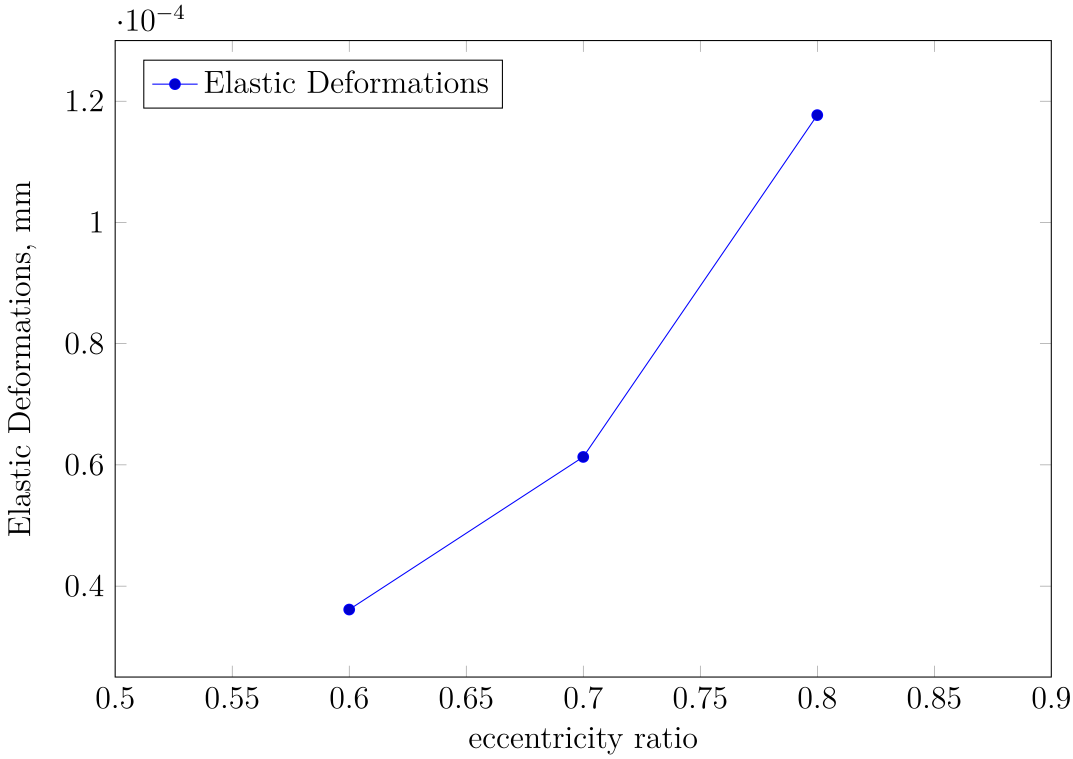

Figure 4.16: Elastic deformations as a function of eccentricity ratio

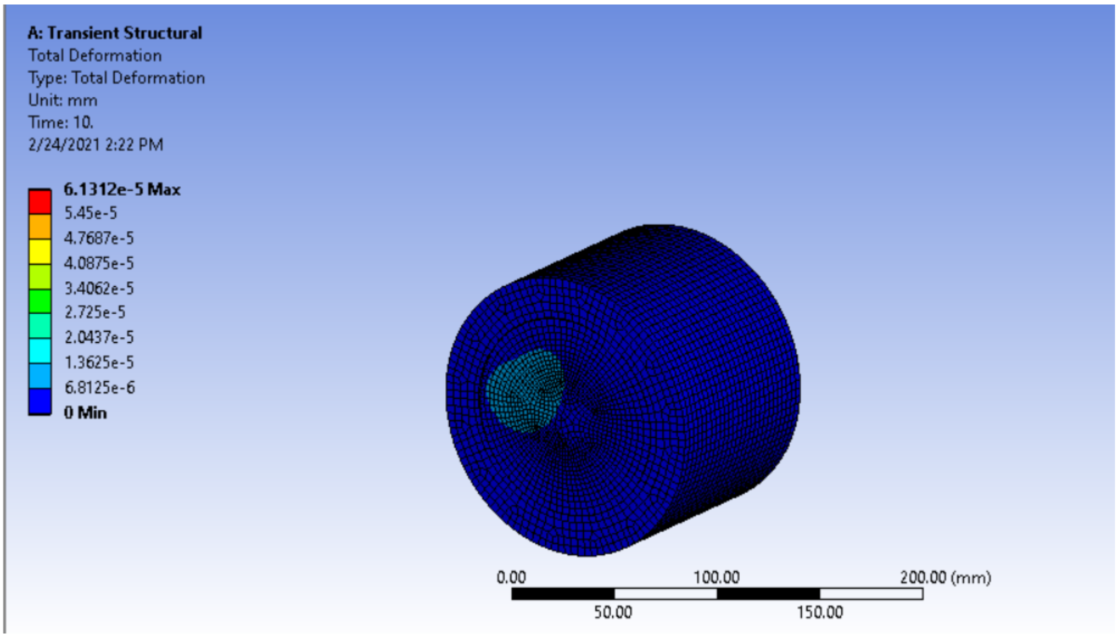

Figure 4.17: Elastic deformation for shaft and bearing at 2500 rpm and 0.7 eccentricity ratio

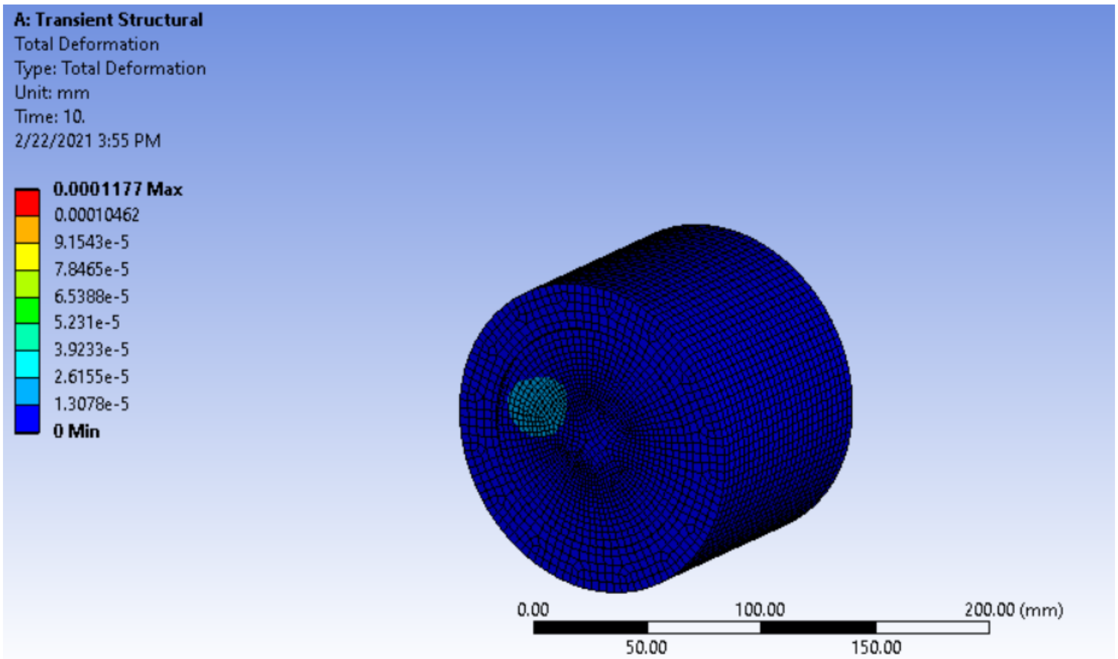

Figure 4.18: Elastic deformation for shaft and bearing at 2500 rpm and 0.8 eccentricity ratio

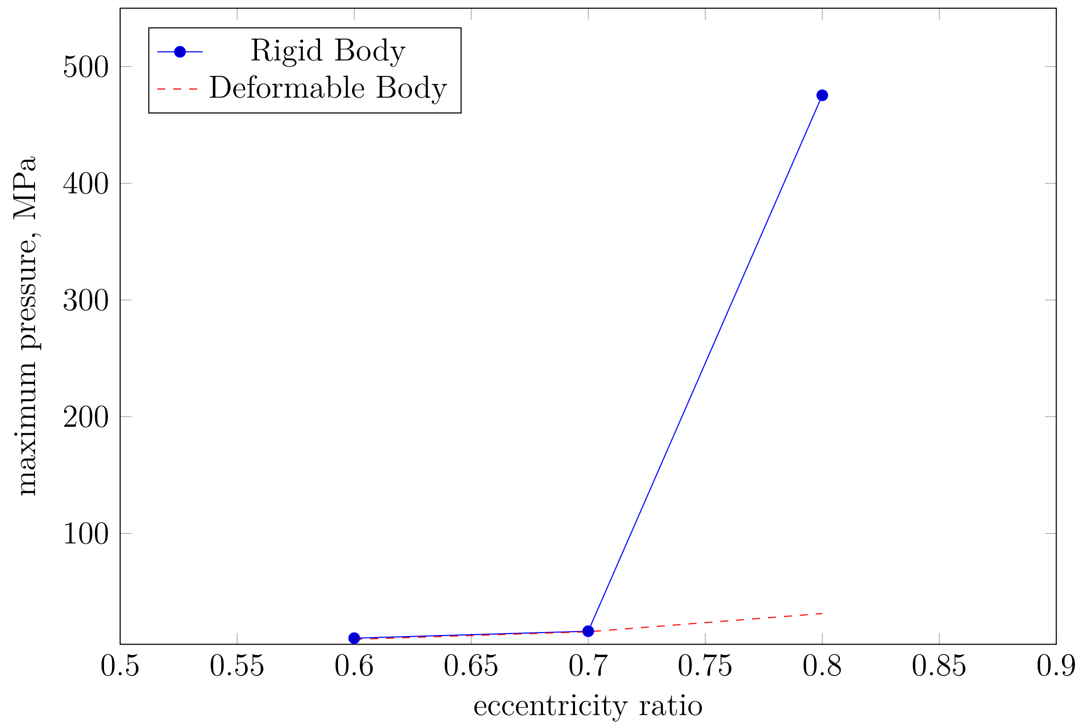

Figure 4.19: Maximum Pressure as function of eccentricity ratio

Chapter 5

Conclusions

The present work used ANSYS for the analysis of hydrodynamic journal bearings. In order to find the load carrying capacity of the journal bearing, the oil pressure distribution should be found by means of numerical methods. First, the work presented two main cases. The first case considers the shaft and the bearing as rigid bodies, thus neglects the effect of elastic deformations. For the other case, system coupling is used, by which mechanical and CFD solvers work together to find the pressure distribution by considering the shaft and the bearing as deformed bodies. By comparing the results for the two cases, we found that the second case (deformable bodies model) gives more accurate results in terms of maximum pressure and pressure distribution. The rigid bodies model overestimates the maximum pressure, thus it overestimates the load carrying capacity of the bearing. In addition, this model is not valid for high eccentricity ratios; higher than 0.7. On the other side, the computational time is more than 40 times higher in the model of deformable bodies.

The work also studied the effect of increasing the shaft rotational speed on the oil pressure distribution for the two models. We found that the maximum pressure linearly increases with the increase of the shaft rotational speed for the two models. Furthermore, the deformable bodies model gave more accurate results, and the percentage of error showed a small decrease between the two models as rpm increases.

Then the work studied the effect of increasing the eccentricity ratio on the oil pressure distribution, and also for the two presented models. The maximum pressure for the two models increased with increasing the eccentricity ratio. The deformable bodies model gave more accurate results for eccentricity ratios lower than 0.8. Whereas, at these eccentricity ratios, the rigid bodies model gave less accurate results, but they are reasonable compared to the results of the other model. While for higher eccentricity ratio, 0.8, the results can be only obtained using deformable bodies model.

Bibliography

[1] Jiří Tůma, Jiří Šimek, Jaromír Škuta, and Jaroslav Los. «Active vibrations control of journal bearings with the use of piezoactuators». In: *Mechanical Systems and Signal Processing* 36.2 (2013), pp. 618–629. DOI: `10.1016/j.ymssp.2012.11.010` (cit. on p. 1).

[2] D. Benasciutti, M. Gallina, M. Gh. Munteanu, and F. Flumian. «A numerical approach for the analysis of deformable journal bearings». In: *Frattura ed Integrità Strutturale* 6.21 (2012), pp. 37–45. DOI: `10.3221/igf-esis.21.05` (cit. on pp. 1, 9, 10).

[3] M. Geller, C. Schemmann, and N. Kluck. «Simulation of radial journal bearings using the FSI approach and a multi-phase model with integrated cavitation». In: *Progress in Computational Fluid Dynamics, An International Journal* 14.1 (2014), p. 14. DOI: `10.1504/pcfd.2014.059196` (cit. on pp. 1, 11).

[4] D. Sfyris and A. Chasalevris. «An exact analytical solution of the Reynolds equation for the finite journal bearing lubrication». In: *Tribology International* 55 (2012), pp. 46–58. DOI: `10.1016/j.triboint.2012.05.013` (cit. on p. 1).

[5] Gabriel J. DeSalvo and John A. Swanson. «ANSYS engineering analysis system user's manual. Houston, Pa :Swanson Analysis Systems». In: *Houston, Pa :Swanson Analysis Systems* (1985) (cit. on p. 2).

[6] D.Y. Dhande and D.W. Pande. «Multiphase flow analysis of hydrodynamic journal bearing using CFD coupled Fluid Structure Interaction considering cavitation». In: *Journal of King Saud University - Engineering Sciences* 30.4 (2018), pp. 345–354. DOI: `10.1016/j.jksues.2016.09.001` (cit. on pp. 2, 11, 16).

[7] Hamid Sadabadi and Amir Sanati Nezhad. «Nanofluids for Performance Improvement of Heavy Machinery Journal Bearings: A Simulation Study». In: *Nanomaterials* 10.11 (2020), p. 2120. DOI: `10.3390/nano10112120` (cit. on pp. 4, 5).

[8] Farooq Ahmad Najar and G. A. Harmain. «Numerical Investigation of Pressure Profile in Hydrodynamic Lubrication Thrust Bearing». In: (2021) (cit. on p. 17).

[9] «Coupling transient mixed lubrication and wear for journal bearing modeling». In: *Tribology International* 138 (). DOI: `10.1016/j.triboint.2019.05.011` (cit. on p. 4).

[10] Luis San Andre´s and Tae Ho Kim. «Improvements to the Analysis of Gas Foil Bearings: Integration of Top Foil 1D and 2D Structural Models». In: *Volume 5: Turbo Expo 2007* (2007). DOI: `10.1115/gt2007-27249` (cit. on p. 6).

[11] Alex de Kraker, Ron A. J. van Ostayen, A. van Beek, and Daniel J. Rixen. «A Multiscale Method Modeling Surface Texture Effects». In: *Journal of Tribology* 129.2 (2006), pp. 221–230. DOI: `10.1115/1.2540156` (cit. on p. 6).

[12] Zhi Lan Chen and Jun Zhu. «Comparison with Thermo Hydrodynamic Lubrication between 2D and 3D Model in Thrust Bearing by Computing Simulation». In: *Advanced Materials Research* 129-131 (2010), pp. 1336–1340. DOI: `10.4028/www.scientific.net/amr.129-131.1336` (cit. on pp. 6, 11).

[13] Marcus Schmidt, Peter Reinke, and Tom Beckmann. «Numerical simulation of suction cavitation in hydrodynamic journal bearings». In: *PAMM* 19.1 (2019). DOI: `10.1002/pamm.201900202` (cit. on pp. 6, 8).

[14] Amit Singla, Abhay Kumar, Saroj Bala, Paramjit Singh, and Amit Chauhan. «Thermo-hydrodynamic analysis on temperature profile of circular journal bearing using computational fluid dynamics». In: *2014 Recent Advances in Engineering and Computational Sciences (RAECS)* (2014). DOI: `10.1109/raecs.2014.6799595` (cit. on p. 8).

[15] Amit Chauhan, Amit Singla, Narender Panwar, and Prashant Jindal. «CFD Based Thermo-Hydrodynamic Analysis of Circular Journal Bearing». In: *International Journal of Advanced Mechanical Engineering* 4.5 (2014), pp. 475–482. URL: `http://www.ripublication.com` (cit. on p. 8).

[16] Aki Linjamaa, Arto Lehtovaara, Roland Larsson, Marke Kallio, and Sven Söchting. «Modelling and analysis of elastic and thermal deformations of a hybrid journal bearing». In: *Tribology International* 118 (2018), pp. 451–457. DOI: `10.1016/j.triboint.2017.02.029` (cit. on p. 8).

[17] K. R. Kadam, Dr. S. S. Banwait, and Dr. S. C. Laroiya. «The Influence of Modified Viscosity-Temperature Equation on Thermohydrodynamic Analysis of Plain Journal Bearing». In: *American Journal of Mechanical Engineering* 2.6 (2014), pp. 169–177. DOI: `10.12691/ajme-2-6-4` (cit. on p. 8).

[18] Hulin Li, Yanzhen Wang, Ning Zhong, Yonghong Chen, and Zhongwei Yin. «Study on the performance of journal bearings in different lubricants by CFD and FSI method with thermal effect and cavitation». In: *MATEC Web of Conferences* 249 (2018), p. 03006. DOI: 10.1051/matecconf/201824903006 (cit. on p. 8).

[19] Philip Croné, Andreas Almqvist, and Roland Larsson. «Thermal Turbulent Flow in Leading Edge Grooved and Conventional Tilting Pad Journal Bearing Segments—A Comparative Study». In: *Lubricants* 6.4 (2018), p. 97. DOI: 10.3390/lubricants6040097 (cit. on p. 12).

[20] L. Bouard, M. Fillon, and J. Frêne. «Comparison between three turbulent models — application to thermohydrodynamic performances of tilting-pad journal bearings». In: *Tribology International* 29.1 (1996), pp. 11–18. DOI: 10.1016/0301-679x(95)00028-3 (cit. on p. 12).

[21] Aoshuang Ding, Xiaodong Ren, Xuesong Li, and Chunwei Gu. «Numerical Investigation of Turbulence Models for a Superlaminar Journal Bearing». In: *Advances in Tribology* 2018 (2018), pp. 1–14. DOI: 10.1155/2018/2841303 (cit. on p. 12).

[22] Sang Myung Chun. «Aeration effects on the performance of a turbocharger journal bearing». In: *Tribology International* 41.4 (2008), pp. 296–306. DOI: 10.1016/j.triboint.2007.08.006 (cit. on p. 12).

[23] Susilowati, Mohammad Tauviqirrahman, J. Jamari, Athanasius P. Bayuseno, and Muchammad. «A Comparative Study of Finite Journal Bearing in Laminar and Turbulent Regimes Using CFD (Computational Fluid Dynamic)». In: *MATEC Web of Conferences* 58 (2016), p. 04001. DOI: 10.1051/matecconf/20165804001 (cit. on p. 12).

[24] B. Manshoor, M. Jaat, Zaman Izzuddin, and Khalid Amir. «CFD Analysis of Thin Film Lubricated Journal Bearing». In: *Procedia Engineering* 68 (2013), pp. 56–62. DOI: 10.1016/j.proeng.2013.12.147 (cit. on p. 14).

[25] Haifeng Wang, Shuyan Yang, and Feng Guo. «Modeling of a Grooved Parallel Bearing with a Mass-Conserving Cavitation Algorithm». In: *Tribology Transactions* 54.2 (2011), pp. 227–236. DOI: 10.1080/10402004.2010.536613.

[26] J. D. Knight and A. J. Niewiarowski. «Effects of Two Film Rupture Models on the Thermal Analysis of a Journal Bearing». In: *Journal of Tribology* 112.2 (1990), pp. 183–188. DOI: 10.1115/1.2920240 (cit. on p. 16).

[27] FM Meng and T Yang. «Preliminary study on mechanism of cavitation in lubricant of textured sliding bearing». In: *Proceedings of the Institution of Mechanical Engineers, Part J: Journal of Engineering Tribology* 227.7 (2013), pp. 695–708. DOI: 10.1177/1350650112468560 (cit. on p. 16).

[28] K. Mehala, N. Bendaoud, and A. Youcefi. «Numerical Analyses of the Non-Newtonian Flow Performance and Thermal Effect on a Bearing Coated with a High Tin Content». In: *Tribology in Industry* 38.4 (2016), pp. 575–584. URL: `http://www.tribology.fink.rs` (cit. on p. 19).

[29] S.P. Tayal, R. Sinhasan, and D.V. Singh. «Analysis of hydrodynamic journal bearings having non-Newtonian lubricants». In: *Tribology International* 15.1 (1982), pp. 17–21. DOI: `10.1016/0301-679x(82)90103-7` (cit. on p. 19).

[30] Abdessamed Nessil, Salah Larbi, Hacene Belhaneche, and Maamar Malki. *Journal Bearings Lubrication Aspect Analysis Using Non-Newtonian Fluids*. 2021 (cit. on p. 19).

[31] S Fialová, M Kozubková, J Jablonská, M Havlásek, F Pochylý, and D Šedivý. «Journal bearing with non-Newtonian fluid in the area of Taylor vortices». In: *IOP Conference Series: Earth and Environmental Science* 240 (2019), p. 062013. DOI: `10.1088/1755-1315/240/6/062013` (cit. on p. 19).

[32] D. Rh. Gwynllyw, A. R. Davies, and T. N. Phillips. «On the effects of a piezoviscous lubricant on the dynamics of a journal bearing». In: *Journal of Rheology* 40.6 (1996), pp. 1239–1266. DOI: `10.1122/1.550782` (cit. on p. 19).

[33] Mukesh Sahu, Ashish Kumar Giri, and Ashish Das. «Thermohydrodynamic Analysis of a Journal Bearing Using CFD as a Tool». In: *International Journal of Scientific and Research Publications* 2.9 (2012).

[34] Saša Bukovnik, Nicole Dörr, Valdas Čaika, Wilfried J. Bartz, and Bernhard Loibnegger. «Analysis of diverse simulation models for combustion engine journal bearings and the influence of oil condition». In: *Tribology International* 39.8 (2006), pp. 820–826. DOI: `10.1016/j.triboint.2005.07.023` (cit. on p. 20).

[35] Ravindra Mane and Sandeep Soni. «Analysis of Hydrodynamic Plain Journal Bearing». In: *Sardar Vallabhbhai National Institute of Technology* (2013).

[36] P. Monmousseau, M. Fillon, and J. Fre^ne. «Transient Thermoelastohydrodynamic Study of Tilting-Pad Journal Bearings Under Dynamic Loading». In: *Journal of Engineering for Gas Turbines and Power* 120.2 (1998), pp. 405–409. DOI: `10.1115/1.2818137`.

[37] V.M. Kulkarni and Manojkumar Udgire. «Computational fluid flow analysis of elasto hydro-dynamic lubrication journal bearing». In: *Integrated Research Advances* 3.2 (2016), pp. 47–52 (cit. on p. 20).

[38] Fabrizio Stefani. «FEM Applied to Hydrodynamic Bearing Design». In: *New Tribological Ways* (2011). DOI: `10.5772/15525` (cit. on p. 20).

[39] Junho Suh and Alan Palazzolo. «Three-Dimensional Dynamic Model of TEHD Tilting-Pad Journal Bearing—Part I: Theoretical Modeling». In: *Journal of Tribology* 137.4 (2015). DOI: 10.1115/1.4030020 (cit. on p. 21).

[40] Sung-Hwa Jeung, Junho Suh, and Hyun Sik Yoon. «Performance of Tilting Pad Journal Bearings with the Same Sommerfeld Number». In: *Applied Sciences* 10.10 (2020), p. 3529. DOI: 10.3390/app10103529.

[41] Hirotoshi Arihara, Yuki Kameyama, Yoshitaka Baba, and Luis San Andrés. «A Thermoelastohydrodynamic Analysis for the Static Performance of High-Speed—Heavy Load Tilting-Pad Journal Bearing Operating in the Turbulent Flow Regime and Comparisons to Test Data». In: *Journal of Engineering for Gas Turbines and Power* 141.2 (2018). DOI: 10.1115/1.4041130.

[42] Fanghui Shi and Qian (Jane) Wang. «A Mixed-TEHD Model for Journal-Bearing Conformal Contacts—Part I: Model Formulation and Approximation of Heat Transfer Considering Asperity Contact». In: *Journal of Tribology* 120.2 (1998), pp. 198–205. DOI: 10.1115/1.2834410 (cit. on p. 21).

[43] Qian Wang. «Seizure failure of journal-bearing conformal contacts». In: *Wear* 210.1-2 (1997), pp. 8–16. DOI: 10.1016/s0043-1648(97)00064-1 (cit. on p. 21).